Chapter 9
Feedback Control of Microflows

Mike Armani, Zach Cummins, Jian Gong, Pramod Mathai, Roland Probst, Chad Ropp, Edo Waks, Shawn Walker, and Benjamin Shapiro

9.1 Introduction

Microfluidics refers to fluid flow inside systems whose features range in size from millimeters to micrometers. This length scale matches the size of biological entities. Consequently, many microfluidic systems are aimed at biochemical applications and some of these have now progressed to medical and clinical use. Under development

M. Armani
Fischell Department of Bioengineering, University of Maryland, and Pathogenetics Unit, Laboratory of Pathology, National Cancer Institute, Bethesda, MD.
e-mail: armanimd@mail.nih.gov

Z. Cummins • R. Probst
Fischell Department of Bioengineering, University of Maryland, College Park MD, USA

J. Gong
Micromanufacturing Laboratory, University of California, Los Angeles, CA, USA

P. Mathai
Aerospace Engineering, University of Maryland, College Park MD, USA

C. Ropp
Electrical Engineering, University of Maryland, College Park MD, USA

E. Waks
Electrical Engineering & Institute for Research in Electronics and Applied Physics (IREAP), University of Maryland, College Park MD, USA

S. Walker
Department of Mathematics & Center for Computation and Technology (CCT), Louisiana State University, Baton Rouge, LA, USA

B. Shapiro (✉)
Fischell Department of Bioengineering & Institute for Systems Research, University of Maryland, College Park MD, USA
e-mail: benshap@umd.edu

and demonstrated biomedical applications include microarrays for rapid analysis of DNA [1, 2], analysis and detection of proteins [3], monitoring and analysis of cells [4], and implantable drug injection systems [5].

Creating, or fabricating, microscale and microfluidic systems is a large and active research area with significant portions of journals (e.g., the *Journal of Micro-Electro-Mechanical-Systems* and *Lab-on-a-Chip*), conferences (Micro-Total Analysis Systems [μTAS]; Hilton Head Sensors, Actuators and Micro-Systems; and the MEMS conference), and books [6–8] devoted to it. MEMS fabrication methods are usually based on lithography – the process of shining radiation (most easily light) through masks onto photosensitive materials to then etch out or build up material layers of the system [9]. The wavelength of light ($\lambda \approx 0.5\,\mu m$) limits the minimum size of the features that can be produced in this way, thus the term *micro* in micro-electro-mechanical-systems. Shorter wavelength radiation (such as electron beams) or other fabrication methods (such as controlled atomistic growth for carbon nanotubes [10] or self-assembly [11, 12]) can enable fabrication of nanoscale features. Generally, lithography fabrication techniques are grouped into methods for rigid substrates, e.g., for silicon and glass (e.g., see [9]), versus methods for polymer materials (soft lithography) [8, 13, 14]. Fabrication often requires deep expertise and dedicated clean-room facilities with expensive machines for each aspect of a fabrication process yet, in some cases, it can be achieved by nonexperts working on a bench top. In fact, there is a spectrum of fabrication capabilities from one to the other, with the former usually needed for smallest feature sizes, hard materials, mirror smooth finishes, and high aspect ratio (thin and deep) features; the latter applying more to soft materials, larger features, and inexpensive (e.g., disposable) systems.

The physics inside microfluidic devices is diverse. Even though momentum effects are usually negligible in microfluidic systems, which means the computationally complex Navier–Stokes equations [15] reduce to the far simpler (linear) Stokes equations (see [16–20]), and even though noncontinuum effects are not yet evident in bulk microscale flows (for example, the mean free path of water is $<1\,nm$ [21] which is still negligible compared to $\geq 1\,\mu m$ device length scales), this does not mean microscale fluid dynamics is easier to understand, model, or quantify than macroscale fluid flow. The complexity is just in different areas: it is in the boundary conditions (the actuation of a fluid by electrically modifying surface tension), in the mix between continuum and discrete elements (cells or DNA chains undergoing Brownian motion in a moving continuous bulk fluid), in the complexity of the bulk fluid itself (in the non-Newtonian behavior of blood), and in the interaction of hundreds or thousands of different fluid samples on a single chip which microfluidic systems allow. Even behavior that is simpler on the microscale takes some time getting used to. Experiments that show that there is no convective (turbulent) mixing on the microscale, the classic T-junction experiments where a green and blue fluid enter each of the T inputs and exit the T output as unmixed half green/half blue [22], are still counter-intuitive even to microfluidic experts. Mixing, which is achieved naturally on the macroscale, becomes an issue that must be solved artificially on the microscale [23–25].

Feedback control is needed in microfluidic applications for the same reasons that it is required on the macroscale [26–28]: to create new capabilities and to enable high performance in the face of uncertainty. Microsystems often operate in largely unknown environments and can have significant geometric, parametric, and dynamic uncertainty. Outside environments may contain unknown biochemical species (as in sensing applications where the presence of rare species must be reliably detected against a background of other common, diverse, and widely varying species); biological fluid samples have a large degree of variability (urine samples vary with disease, with hydration, and from patient to patient), and the characteristics of specific entities inside the samples can vary (cells of the same type will have different shapes and properties). Device geometric uncertainty is created by fabrication limits: the wavelength of light limits lithography resolution to ∼0.5 µm, hence devices with 5 µm sized features will have a >10% variability in geometry. Finally, mathematical models that characterize biochemical behavior (such as models of surface tension boundary conditions, reaction rates, diffusion, migration, species adsorption, and desorption) contain uncertain parameters and unmodeled effects. The system design that necessarily relies on these models must be made insensitive to the errors that they contain. Feedback is required to address all of these uncertainties and to create robust behavior, enable new tasks, and improve system performance.

To illustrate results and challenges this chapter includes two broad examples. The first deals with control of fluid packets on chip using electrically modulated surface tension forces (in collaboration with UCLA). The second provides results on steering of individual particles (cells and quantum dots) by microflow control. In both cases, we show how feedback control can improve performance and enable new capabilities.

These two examples illustrate common challenges encountered by us, in these and other projects, and they closely match the challenges encountered by others (as evidenced by the recurrence of the same issues from chapter to chapter in this book). Broadly, these challenges are: choice of problem (which need should the microscale system address?), fabrication (build it), physics (which phenomena occur?), modeling (describing the physics by equations and then quantifying their solution by numerical methods), control (problem definition, the more critical aspect, and subsequently problem solution), experimental verification, and validation.

A thread that runs through all of the preceding aspects is multidisciplinary communication, or, more accurately, multidisciplinary training and collaboration. We have found time and again that we can only create working systems once we have deeply understood the needs, physics, numerics, and experiments for that application, or, alternately, once each of those areas of expertise is represented in the research team. Being a controls expert just *talking* to a MEMS expert or a clinician is almost always not good enough. The clinician must be willing to become a part of the team. The reverse is likely also true: being a MEMS expert and talking to a controls expert is insufficient, rather, the microsystems expert or clinician should find the right controls person and make him or her a part of the research program.

9.2 Control for Electrowetting Actuation

Electrowetting refers to the local modification of surface tension by electric actuation to manipulate liquid droplets on the microscale [29–41] (Fig. 9.1). By applying electric fields via actuating electrodes, surface tension and electrical effects compete [29, 42, 43], and this competition can create forces that vary in both space and time and that can be used to move, split, merge, shape, and mix fluids in microscale devices. The size of the manipulated droplets usually roughly matches the size of the electrodes (as shown below), or is larger, to permit each droplet to contact multiple electrodes and thus be actuated in different directions.

Applications of electrowetting include re-programmable lab-on-a-chip systems [30, 31], auto-focus cell phone lenses [37] (commercially marketed by Varioptic), and the development of colored oil pixels for laptop screens and flexible video-speed "smart paper" [34–36] (under development by Liquavista).

9.2.1 Modeling

Our control design for electrowetting has benefited dramatically from, and in fact has been permitted by, the system modeling that we have carried out. The modeling that is needed must be sufficiently rich to capture the basic physics but sufficiently compact (or, more subtly, in a form that is suitable) for control design – the models must be *useable* in conjunction with available control analysis and synthesis techniques [27, 28, 46, 47]. Modeling is essential and still useful for our control design even though we work with complex and messy systems that we know we cannot fully capture mathematically – both because we do not know all the physics and because each physical phenomena will have aspects (such as the detailed chemistry of surface tension) which are outside our reach. Feedback allows us to manage the uncertainty in our models. Essentially, our models must be good enough to tell us how to actuate to make things better – to push the fluid from where it is to closer to where it should be. In both the electrowetting example and in the electro-osmotic flow control that follows, this is sufficient to control the fluid in dramatic ways and the objects within it to startling accuracy.
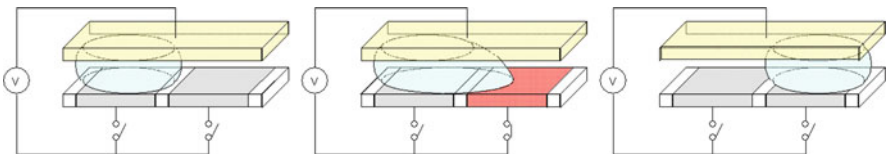
Fig. 9.1 An example of electrowetting actuation (schematic). The activated electrode (*red pad*) effectively and locally decreases the surface tension of the liquid above it, causing it to move to the right [44, 45]. (Used with permission. Copyright John Wiley & Sons, Ltd; American Institute of Physics)
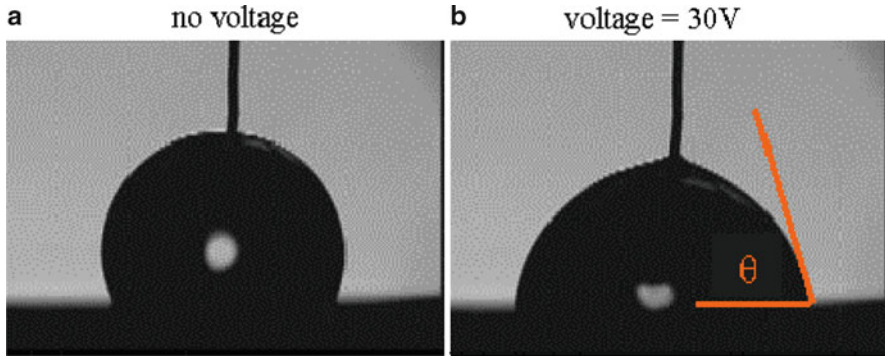
Fig. 9.2 In the simplest example of electrowetting, an applied voltage changes the shape of a liquid droplet. The figure shows the induced change in the contact angle of a droplet of deionized, distilled water (pH 6.5) on 50 nm thick Teflon AF coating a 120 nm thick silicon dioxide dielectric layer. An applied voltage of 30 V between the inserted platinum wire and underlying gold electrode causes the droplet to flatten reversibly [44]. (Used with permission. Copyright John Wiley & Sons, Ltd)
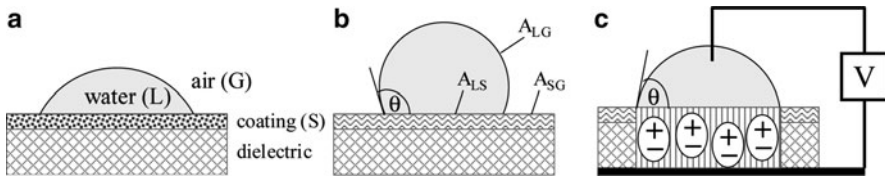
Fig. 9.3 Electrowetting shape change actuation: a competition between surface tension and dielectric energy. (**a**) A drop of water on a hydrophilic surface. The liquid/solid energy per unit area is low, and so the drop prefers a shape with a high (low penalty) liquid/solid area and a lower (higher penalty) liquid/gas area at its energy minimum (equilibrium). (**b**) The same drop on a hydrophobic surface. The contact angle θ and the liquid/solid, liquid/gas, and solid/gas interface areas are marked. (**c**) The drop of (b) with voltage actuation. The resulting charged solid volume is marked by the $\pm$ dipoles. Surface tension penalizes the liquid/solid area, but the dielectric energy in the charged volume (and the voltage source) rewards an increase in this area. The $\pm$ charges in the dielectric lead to a surface charge (here $+$) at the solid/liquid surface. (A schematic two-dimensional slice is shown. The figure is not to scale, the solid is very thin)

At the core of electrowetting is a competition between surface tension and dielectric energy. As noted in the review by Mugele and Baret [29], there is now a basic agreement that this is the dominant physical cause, and, at equilibrium, this competition can be quantified either by classical thermodynamics, an energy minimization, or a force balance electromechanical approach. All of these yield the same classical Young–Lippmann equation which predicts, to first order, the shape (contact angle θ, Fig. 9.2) of a single droplet as a function of the applied voltage [48]. We briefly summarize the energy minimization argument.

Figure 9.3 shows a schematic of the setup and physics for the experiment of Fig. 9.2. At equilibrium, an un-actuated droplet will minimize its total surface tension potential energy (the energy due to gravity is negligible on the microscale).

This energy is composed of the liquid/gas, liquid/solid, and solid/gas interface energies, each of which is given by a surface tension coefficient times that interfacial area [49, 50]. In this view, a water droplet on a hydrophobic surface beads up because its liquid/solid surface tension coefficient is high compared to its liquid/gas coefficient, and the droplet shrinks its L/S area at the expense of a larger L/G area.

When a voltage V is applied, then in addition to surface tension energy there is also an electrical energy. If the liquid is conducting, it stores no electric energy, the applied voltage is transferred to the liquid/solid contact area, and the solid material underneath the liquid is dielectrically charged (Fig. 9.3c). The solid dielectric energy scales as the charged volume, which is equal to the L/S area times the (constant) material thickness. Along with this energy stored in the material, there is also an energy stored in the voltage source. The total energy now becomes [29, 43, 51]:

$$U = \left(\sigma_{\mathrm{LS}} - \sigma_{\mathrm{SG}} - \varepsilon_{\mathrm{S}} V^2/2h\right) A_{\mathrm{LS}} + \sigma_{\mathrm{LG}} A_{\mathrm{LG}}, \tag{9.1}$$

where σ_{XY} are the surface tension coefficients, A_{XY} are the interface areas, L, S, and G denote liquid, solid, and gas, ε_{S} is the dielectric constant of the solid and h is its thickness. This is the new energy that must be minimized by the liquid shape and it alters the classical Young energy minimum [43, 49, 50] to the Young–Lippmann minimum [48]:

$$\cos\theta = -\left(\sigma_{\mathrm{LS}} - \sigma_{\mathrm{SG}} - \varepsilon_{\mathrm{S}} V^2/2h\right)/\sigma_{\mathrm{LG}}. \tag{9.2}$$

In this way the applied voltage V changes the contact angle θ, i.e., the shape, of the liquid droplet.

Our interest is in controlling the *dynamics* of electrowetting, so beyond equilibrium, we require models for the fluid dynamics. As stated earlier, our modeling must capture the essential physics but still be tractable (computationally cheap, of a suitable form) for control design. Our prior dynamic modeling efforts [19, 45, 52] have focused on the UCLA electrowetting system, a planar liquid-in-air electrowetting-on-dielectric (EWOD) system [30, 31, 39] (Fig. 9.4). (Also see Lu et al. [53].) For dynamic modeling of EWOD, the critical aspects are the low Reynolds number fluid dynamics of the bulk liquid (water, glycerine, etc.), the liquid/air boundary conditions, numerical methods for tracking the moving liquid/air interfaces and enforcing appropriate boundary conditions, as well as incorporating loss mechanisms such as contact angle saturation, contact line hysteresis and pinning/de-pinning which limit system performance [29].

We model the bulk fluid flow by simplifying the Navier–Stokes equations. The continuum assumptions behind the NS equations remain valid because the micrometer device length scales are still far greater than the mean free path of both air and water molecules [16]. Because we are modeling the flow of water or glycerine, incompressibility and Newtonian fluid assumptions also hold [15]. At low Reynolds numbers, for flow of liquid surrounded by air between two narrowly spaced plates (Fig. 9.5), the Navier–Stokes equations reduce to the Hele-Shaw equations [54, 55], with a pressure boundary condition given by the Young–Laplace
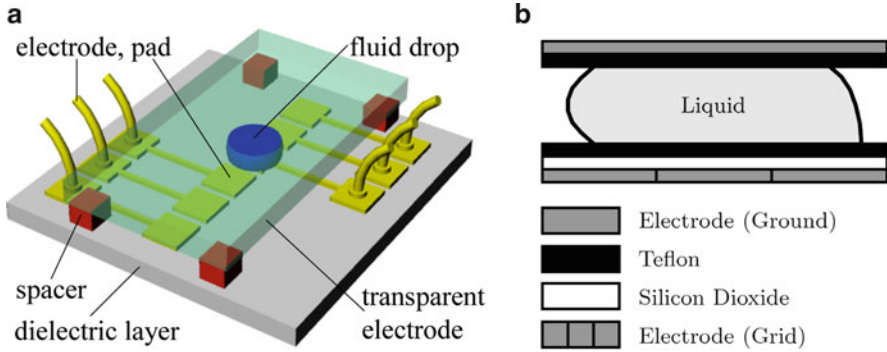
Fig. 9.4 The UCLA EWOD system. (**a**) Schematic. (**b**) Cross-section view [19, 45]. (Used with permission. Copyright IEEE, American Institute of Physics)

Fig. 9.5 Liquid flow in a Hele-Shaw cell: the fluid velocity field is assumed to have a quadratic profile in the z-direction [19]. (Used with permission. Copyright IEEE)
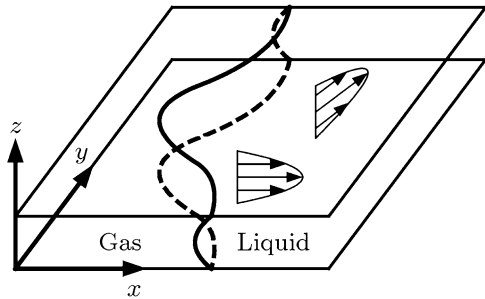
relation at the liquid/gas interface. Thus the two-dimensional fluid equations inside (the possibly many) droplets actuated by EWOD are given in nondimensional form as (see [19, 45, 52] for details):

$$\alpha \frac{\partial \vec{u}}{\partial t} + \beta \, \vec{u} + \nabla p = 0, \quad \text{in } \Omega$$

$$\nabla^2 p = 0, \quad \text{in } \Omega, \qquad (9.3)$$

where Ω is the domain of the liquid, $\vec{u}$ is the two-dimensional vector velocity field (in the plane of the device), and p is the pressure. The nondimensional constants α and β depend on the fluid parameters and the geometry of the device:

$$\alpha = \left(\frac{\rho L U_0}{\mu} \right) \text{Ca}, \qquad \beta = 12 \left(\frac{L}{H} \right)^2 \text{Ca}, \qquad \text{Ca} = \frac{\mu U_0}{\sigma_{\text{LG}}},$$

where ρ is the fluid density, H is the height between the parallel plates, L is the planar liquid length scale (e.g., the pitch of the EWOD electrodes), U_0 is the velocity scale, μ is the dynamic viscosity, Ca is the capillary number (the ratio of viscosity

versus surface tension forces), and σ_{LG} is the surface tension coefficient of the liquid/air interface. The time derivative term in (9.3) is nonstandard, usually it is negligible in microflows, but it is included here because fast actuation of the EWOD electrodes can lead to an imposed fast time-scale making local momentum effects (the $\partial \vec{u}/\partial t$ term) appreciable. The convective momentum term $(\vec{u} \cdot \nabla)\,\vec{u}$ in the Navier–Stokes equations remains negligible even with fast EWOD actuation (see [19] for details) and so does not appear in our model. Crucially for control design (see the next section) this means the bulk fluid equations are linear from pressure to velocity.

Boundary conditions at the liquid/air interface drive the bulk flow. These conditions include surface tension, electrowetting actuation (which is really a competition between dielectric and surface tension energy as described above but effectively acts at the liquid/gas interface), electrowetting loss-phenomena (such as contact angle saturation), and pinning and de-pinning of the triple line (the moving liquid/gas/solid interface). A portion of these effects can be written in a straightforward way, in particular surface tension [49, 50] and ideal electrowetting actuation [29, 48] have standard descriptions, but interface loss-phenomena, such as contact angle saturation and triple line pinning, are subtle, depend on fine scale physics and chemistry, vary from system to system, and remain the subjects of fierce debate.

Surface tension creates a pressure jump across curved interfaces [49, 50], this pressure jump is quantified by the classic Young–Laplace relation [55]:

$$\Delta \tilde{p} = \sigma_{LG}(\kappa_1 + \kappa_2), \qquad (9.4)$$

where κ_1 and κ_2 denote the principal curvatures [56] (we have written this equation in dimensional form). In the planar EWOD devices, we can take the principal curvatures to have one direction in the plane of the device and the other along the channel height. After nondimensionalizing and setting the arbitrary outside reference pressure to zero, the nondimensional pressure just inside the liquid/air interface is given by [19]:

$$p = \kappa + \frac{L}{H}\kappa_z, \quad \text{on } \Gamma \qquad (9.5)$$

where $p = \Delta \tilde{p}/\Delta P_0$, κ is the curvature of the liquid/air interface in the plane (the xy curvature), κ_z is the curvature of the interface in the vertical z-direction, and $\Delta P_0 = \sigma_{LG}/L$ is the dimensional pressure scale.

Electrowetting actuation modifies the pressure of (9.5) by bending the interface – it changes κ_z. For a small vertical gap H, which allows us to assume that the liquid/air interface is circular in the vertical direction, there is a direct geometric relation between κ_z and the local top and bottom contact angles θ_t and θ_b. In the UCLA devices, electrodes are placed on the bottom and so it is θ_b that is actuated – whenever an electrode is turned on the local contact angle above it decreases (the liquid spreads out). For applied voltages that cause small or medium changes in contact angle, the relation between the cosine of the angle and the applied voltage

is quadratic ((9.2), the Young–Lippmann relation). But relation (9.2) does not hold indefinitely, at some point further increasing the actuation voltage brings into play non-ideal phenomena that prevent a further decrease in contact angle – this is known as contact angle saturation and is one of the fundamental limits of electrowetting performance. Causes of contact angle saturation are under debate, they vary from system to system [29], and they are difficult to predict from first principles. Thus, in our modeling, we have quantified the relation between the applied voltage V and the resulting contact angle $\theta(V)$ by fitting to experimental data for the UCLA system (see [19, 45]).

In addition to contact angle saturation, there is also contact line pinning. Line pinning is the phenomenon that prevents droplets from sliding down a vertical window pane, it can oppose gravity at zero velocity, its force is not proportional to a fluid shear, and it is, therefore, not a viscous effect per se. Rather, it is a kind of molecular adhesion that occurs at the triple contact line of the droplet [57]. In electrowetting devices it can prevent droplets from returning to a perfectly circular shape when electrowetting actuation is turned off, which is what they would do under surface tension in the absence of pinning. Like contact angle saturation, the physics of contact line pinning is complex and under debate. It is often modeled by fine scale atomistic simulations which are too computationally expensive to be included in models for control. Recently, we proposed a modeling paradigm that includes a simple description and can numerically track pinning [45] but we have not yet carried out control studies for this new modeling capability.

Solving the bulk flow equations with the boundary conditions above (equation (9.5)) yields a flow velocity at each time, and this flow velocity convects the fluid/gas interface Γ as follows. For each point $\vec{x}$ on the interface:

$$\frac{\partial \vec{x}}{\partial t} = \vec{u}(\vec{x}) = \left[\vec{u}(\vec{x}) \cdot \hat{n}(\vec{x})\right] \hat{n}(\vec{x}), \tag{9.6}$$

the velocity of that point is given by the flow velocity at its location. However, since the change in droplet shape is due only to the normal component of the velocity, the second form in (9.6) is also correct, where $\hat{n}$ is the unit outward normal.

To summarize the model, the planar bulk fluid dynamics of the liquid is described by (9.3), the air is ignored, and the liquid/air boundary conditions that drive the bulk flow are given by (9.5). Here κ_z depends on the voltage applied at the electrode underneath that portion of the interface and its dependence on that voltage is identified from experiments. This gives a complete set of equations for the pressure and fluid velocity at each time. The fluid velocity then updates the shape of the liquid by (9.6).

A sound numerical implementation of this model is difficult. The hard part is good numerical tracking of the moving interfaces, which move quickly and undergo topological changes (split and merge events), and accurately computing and applying interface boundary conditions. In particular, surface tension boundary conditions require a clean and robust computation of interface curvature: this
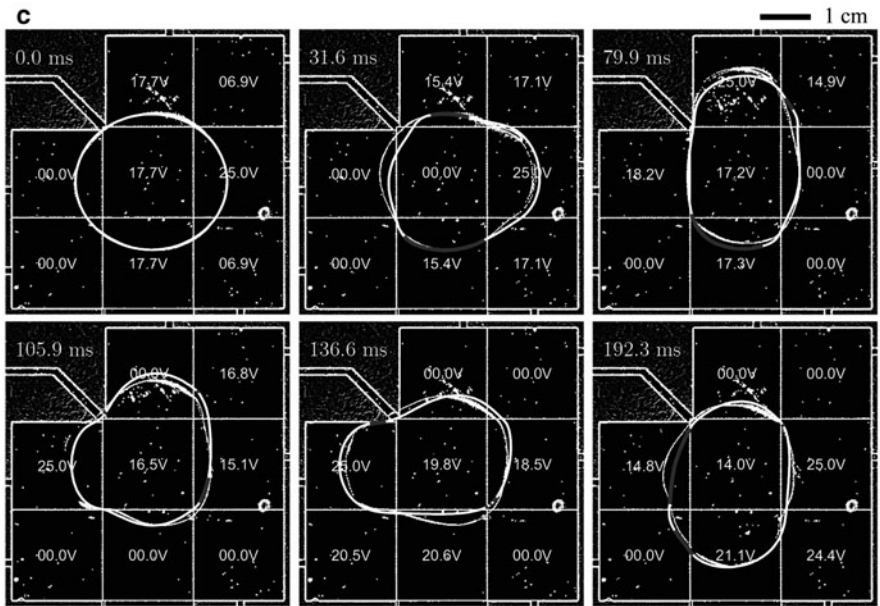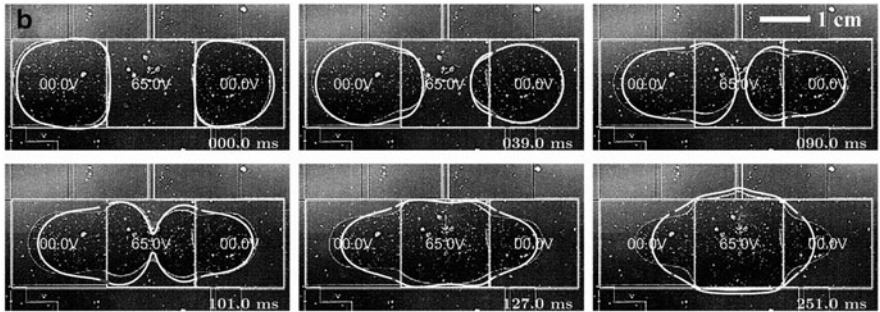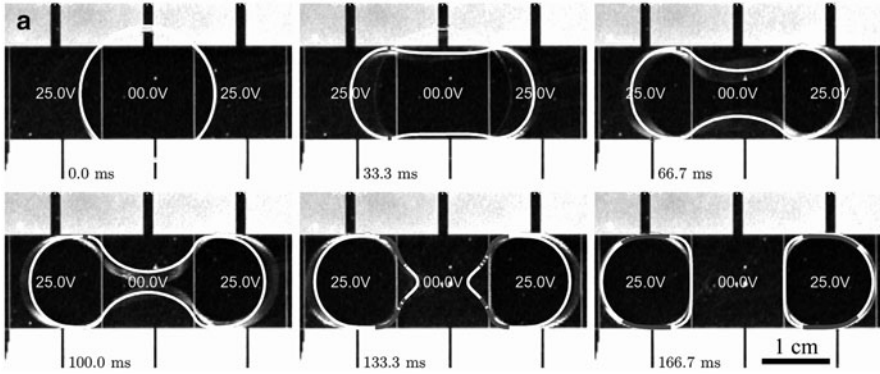
involves a second derivative in space and can lead to large numerical noise if not handled correctly. In our first numerical implementation, we tracked interfaces by a level-set approach [19]. The level-set method implicitly tracks the liquid boundaries as the zero level-set of a scalar function defined on the plane [58–60]. This function is convected by the fluid velocity and so deforms and changes shape – its zero level corresponds to the liquid/gas boundary. In level-set approaches there are issues with computing curvature and enforcing mass conservation. Using an explicit calculation of curvature requires restricting the time-step to be less than the square of the mesh spacing, which can be expensive [58,59]. Computing the curvature implicitly can be done in the level-set framework [61] but is more expensive. Mass conservation is an issue because the standard level-set schemes are not globally conservative, thus they tend to lose mass over the course of a simulation [58,62,63]. This can be alleviated by other techniques [64–66] but they further complicate the method.

In our more recent work [45,52,67], we use a variational front-tracking approach that represents the interface explicitly and solves the underlying PDEs using a variational formulation which is discretized by a finite element method. Our new method has the advantage that it is globally conservative, so mass conservation is not an issue. Here we discretize curvature using a semi-implicit method that is straightforward to implement in our variational approach. In this new method we have to deal with distortion of the underlying finite element mesh and this is especially important in the case of topological changes. But we handle this by a hybrid variational front-tracking level-set approach that is able to take explicit meshes through a pinching/merging event without too much computational overhead [67]. The primary advantage of the level-set method is enabling topological changes and we use it in this way only when we need it (i.e., only where and when a pinch or merge event occurs). Another advantage that our variational approach has is in modeling and computing the effects of contact line pinning which we describe in detail in [45]. Our contact line pinning hybrid method uses a variational inequality to capture the pinning effect – it is not at all obvious how this could be implemented in a pure level-set framework.

Our numerical models evaluate in minutes on a laptop computer and accurately capture behavior observed experimentally in the UCLA EWOD systems. Figure 9.6 shows a representative sample of results (taken from [45]). Our models are fast yet accurate; this makes them amenable to the control design discussed next.

Fig. 9.6 A sample of comparisons between our EWOD model and experimental data from UCLA (from [45]). In all panels, the simulated interface is the *solid curve* (*white* for free, *gray* for locally and transiently pinned), and the experimental interface is visible as a *thin line* that is sometimes motion blurred. The numbers show the voltage applied at that electrode pad. The view is from the top through the top transparent electrode of Fig. 9.4. From top to bottom: (**a**) drop being split into two, (**b**) two drops joining into one, and (**c**) a drop being moved along a complex path. The model includes a simple force–threshold contact line pinning description that enables us to capture, to a degree, the final noncircular pinned shape of the droplet [45]. (Used with permission. Copyright American Institute of Physics)
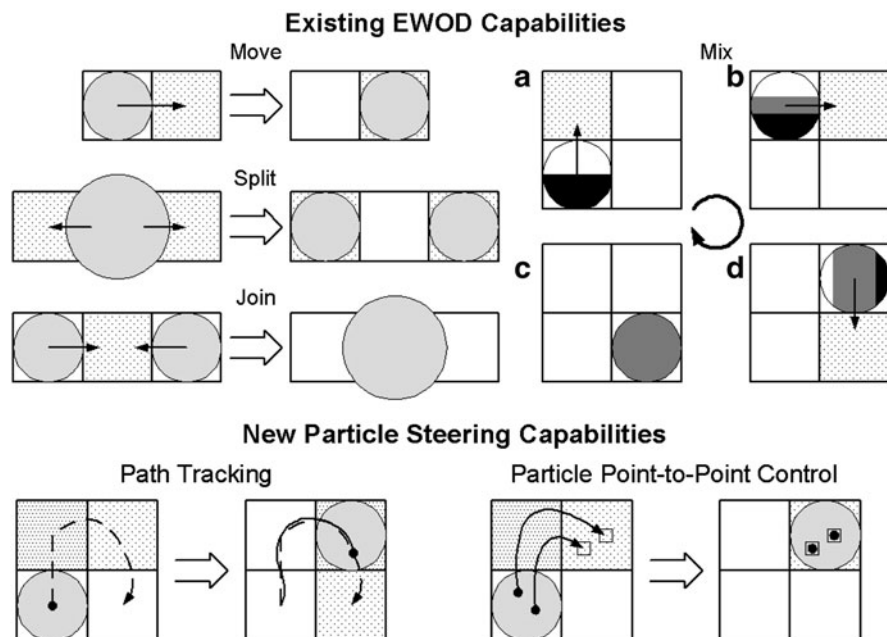
Fig. 9.7 Existing (move, split, join, and mix) capabilities of electrowetting devices are shown schematically above (see [24, 30, 40, 68–71]) alongside the new particle steering capability enabled by the control methods described next. The view is from the top. *Shaded circles* represent droplets of liquid. *Squares* are electrodes where the *dotted hatching* indicates the electrode is on. *Directed lines* specify the direction of motion. The *multishaded* droplet shows the diffusion and mixing of two chemicals, here mixing is enhanced by the fluid dynamics created inside the droplet due to its imposed motion [72]. (Used with permission. Copyright Royal Society of Chemistry)

9.2.2 Control

Current electrowetting systems use simple control scripts but can already perform the key operations outlined in Fig. 9.7 – they can move, split, and join fluid droplets and effectively mix chemicals inside them. Feedback control can improve precision and robustness and our specific results below could enable manipulation of individual particles within single EWOD droplets – a new capability for electrowetting. The control algorithms presented next are based on the EWOD model developed above ((9.3) through (9.6)) but without contact line pinning.

9.2.2.1 Control for Particle Steering

Steering of multiple particles inside EWOD driven droplets, using actuators already available in standard EWOD devices, requires more sophisticated control

of the electrode voltages. The voltages directly influence, through the boundary conditions, the pressure gradient field inside the droplet (see (9.5)). Hence, by manipulating the voltages, we can control the fluid flow fields (9.3), and thereby control the velocities and positions of particles inside the liquid droplets. We consider neutral (uncharged) particles that are simply carried along by the (vertically averaged) planar fluid flow. Thus a particle at the location (x, y) will simply follow the velocity of the fluid at its location:

$$\dot{x} = u(x,y), \qquad \dot{y} = v(x,y), \tag{9.7}$$

where (u, v) is the flow field from (9.3) and the dots denote derivatives with respect to time. Therefore, our control problem is to find electrode voltage sequences that create temporally and spatially varying flow fields that will carry the target particles along their desired trajectories.

The control problem described above is a trajectory-tracking problem: we seek to find the control inputs that will cause the system (in this case the particle positions) to follow a desired trajectory. A naïve inspection of the equations of motion, especially (9.3) for the particle dynamics, would suggest that the control problem is standard in linear control theory and that a linear quadratic regulator (LQR) tracking controller [73] could be used. However, the particle motion depends on the droplet shape and on the number of electrodes that the droplet overlays at any given moment. This information is not known a priori, which means that an LQR approach cannot be used. For this reason, we do local estimation and control at each time-step of our simulation using a least-squares framework to compute the necessary pressure boundary conditions, and then find the electrode voltages that will achieve these boundary pressures. Any particle deviation from the desired trajectory that may arise from thermal fluctuations, external disturbances, and actuation errors is corrected using feedback of the particle's position. Figure 9.8 gives a diagram of the needed closed-loop feedback architecture.

For a single particle, the control algorithm would proceed as follows:

1. Initialization: represent trajectory as a set of points connected by straight lines.
2. Find the particle position and the location of the droplet boundary.
3. Find the closest trajectory point to the particle.
4. Set the particle's desired direction of motion to be toward a nearby next trajectory point.
5. Solve a least-squares problem for the necessary voltage actuation to induce a pressure gradient field that will move the particle along the desired direction of step 4.
6. Apply control voltages, solve for the resulting pressure and fluid velocity, and update the position of all the particles. Advance to the next time-step of the simulation. Go back to step 2 and iterate.

The control algorithm details are described next.
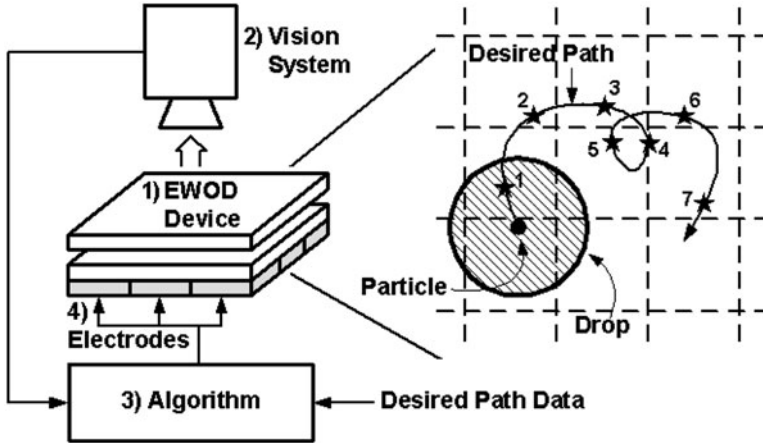
Fig. 9.8 Particle steering closed-loop feedback control architecture. (*1*) The EWOD device will be observed by (*2*) an image system (a microscope/camera or an on-chip contact imager) which transmits information to (*3*) a computer or chip that contains (*3*) an image processing algorithm to identify droplet shapes and the location of the particles and a control algorithm that computes the actuator voltages that will move the particles from where they are to where they should be, and (*4*) these actuation voltages are then applied on the EWOD device. The loop would repeat at each time step to steer the particles along their desired trajectories. The zoomed top view of the EWOD device shows a single droplet with one particle floating inside. The *curvy line* indicates the desired path of the particle. In our simulated control algorithm, we sample the trajectory by many points (only seven points are shown here; see the numbered *stars 1–7*)

Algorithm Initialization

We represent the desired trajectory curve for each particle as a fine sampling of points connected by straight lines. The points are indexed in the order in which the particles should follow them (i.e., the trajectory is parameterized; see Fig. 9.8). Complicated trajectories are broken up into separate segments for ease of particle tracking. For simplicity, only one particle and trajectory is considered in the following sections. Simultaneous multiple particle steering is discussed in the least-squares step.

Particle Position and Droplet Boundary Sensing

We need to know the shape and position of the droplet as well as the position of each particle in order to apply our control algorithm. At the beginning of each time step, we obtain the position of the particle and the location of the droplet boundary using feedback through a vision system (see Fig. 9.8). The issues of integrating a vision system with an EWOD device are not considered here. For the purposes of this chapter, the particle positions and droplet shape information are taken directly from the simulation.

Compute the Desired Direction of Particle Motion

Next, the desired direction of motion for the particle is chosen to be a unit vector that points from the particle's current coordinates toward one of the trajectory points. Since maximum forcing of the pressure gradient is used to drive the particle in the desired direction (see Fig. 9.10), it is necessary to choose a trajectory point that is just out of reach of the particle for the current time step. Otherwise, it is possible that the particle could overshoot trajectory points and trace out an unwanted zigzag path around the trajectory.

Hence, we find the target trajectory point by first finding the closest trajectory point to the particle. Then, using the trajectory parameterization (i.e., the index list; see Fig. 9.8), we look ahead after the closest point and choose the target to be the first trajectory point that is at least one grid spacing away. This ensures the particle will move forward along the trajectory. It also guarantees that the target point is out of reach because the time steps of our simulation are chosen by the CFL criterion [74], which says that no particle can move more than a grid step at each time-step. If the closest trajectory point is the last point of the trajectory, then the particle aims for the last point.

For a self-intersecting or extremely curvy trajectory, it is possible that the particle could become stuck in a loop and not travel the entire trajectory. We resolve this issue by breaking the trajectory into smooth segments that do not intersect and only allow the particle to see one segment at a time. As a result, the particle follows one piece of the trajectory until it reaches the end, where our algorithm switches to the next segment. Therefore, without loss of generality, we assume in the following subsections that the trajectory consists of just one segment.

The forcing of the particle is created by the pressure gradient. And the desired unit vector discussed above determines the direction of forcing. This unit vector is used in the next section to calculate the pressure boundary conditions needed to realize the pressure gradient that will move the particle in the desired direction.

Least-Squares Solution of the Required Pressure Boundary Conditions

Figure 9.9 shows a top view of a sample droplet in the EWOD device containing a single particle. The current drop shape overlaps four electrodes; hence four actuators are available to move the single particle. In each of the four cases, only one electrode is on; the rest are off. The arrows inside the droplet show the fluid flow for each of the four voltage actuations. The black dot represents the particle with a thick arrow indicating the negative direction of the pressure gradient at the particle location (note that the fluid flows opposite to the pressure gradient).

Our algorithm centers on the idea of taking the right linear combination of pressure gradients in Fig. 9.9 to make the particle (or particles) move in the direction(s) we want at a particular time step. This will directly correspond to finding the right combination of electrode voltages at every time step to realize the desired particle motion (or motions).
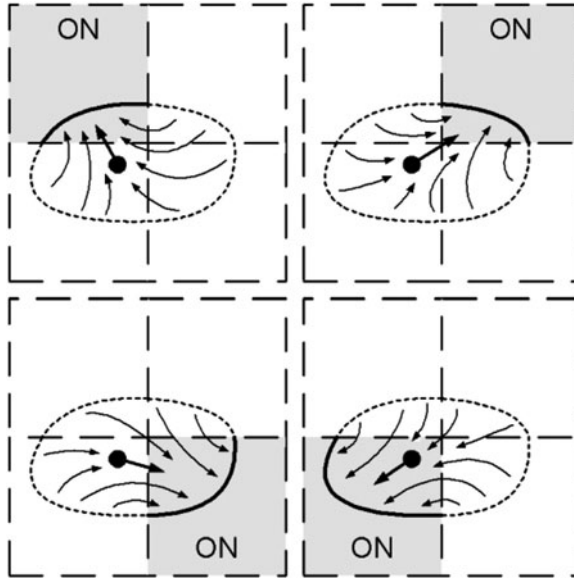
Fig. 9.9 Linear combination of pressure gradients for a single droplet overlaying four electrodes (*small dashed squares*). The diagram above shows a droplet in an EWOD system with four different instances of voltage actuation. In each instance, only one of the four electrodes is on. The particle floating inside the droplet (*black dot*) has a *thick arrow* indicating its direction of motion for each single electrode actuation. These *arrows* actually represent the opposite direction of the pressure gradient when a unit pressure boundary condition is set on the *thick curve* that overlays the *shaded* electrode, with zero pressure boundary conditions everywhere else. The *thin curvy arrows* show the fluid flow inside the droplet. Since the pressure equation (second equation in (9.3)) is linear, we can make the particle move in any desired direction by taking an appropriate linear combination of the four possible boundary conditions given above [72]. (Used with permission. Copyright Royal Society of Chemistry)

First, given the current droplet configuration, we solve the pressure equation in (9.3) for the pressure field inside the droplet for a single active electrode. The pressure boundary conditions are defined to be one on the droplet boundary that lies over the active electrode and zero everywhere else (see Fig. 9.9). From the pressure solution, the pressure gradient at each particle's position is computed. After repeating this for each electrode, we obtain a matrix of pressure gradients:

$$G = - \begin{bmatrix} \nabla P_1(x_1, y_1) & \cdots & \nabla P_N(x_1, y_1) \\ \vdots & \ddots & \vdots \\ \nabla P_1(x_m, y_m) & \cdots & \nabla P_N(x_m, y_m) \end{bmatrix}, \tag{9.8}$$

where (x_j, y_j) are the coordinates for the jth particle. Each column of pressure gradients $\nabla P_k(x_j, y_j)$ in the matrix corresponds to a single active electrode; each row

to a single particle. The total number of particles is m and the number of available electrodes is N. The minus sign accounts for the direction of particle motion.

Next, given the desired pressure gradient at each particle's location in the droplet, we wish to find the appropriate boundary conditions to realize it. Since Laplace's equation for the pressure in (9.3) is linear regardless of the droplet shape, solutions for single active electrodes can be combined linearly to obtain the pressure gradient field due to many active electrodes. This reduces our problem to solving a linear system:

$$G\alpha = b, \alpha = \begin{bmatrix} \alpha_1 \\ \vdots \\ \alpha_N \end{bmatrix}, \quad b = \begin{bmatrix} \nabla P_D(x_1, y_1) \\ \vdots \\ \nabla P_D(x_m, y_m) \end{bmatrix}, \tag{9.9}$$

where $\nabla P_D(x_j, y_j)$ is a 2×1 vector representing the desired pressure gradient at the jth particle and α is the vector of boundary values that will achieve b. We set $\nabla P_D(x_j, y_j)$ equal to the unit vector that represents the desired direction of motion for the jth particle. If $2m \geq N$, the number of particle degrees of freedom is greater than the available actuators and (in general) (9.9) cannot be solved exactly. Then, a least-squares solution is needed to obtain the best fit of actuations α. Otherwise, it is a pseudo-inverse problem, which has a solution as long as the matrix G has full row rank [75].

We solve (9.9) for α using singular value decomposition (SVD) [75]. In addition, each component of the solution vector must be made to satisfy an inequality constraint:

$$\alpha_{\min} \leq \alpha_j \leq \alpha_{\max}, \qquad 1 \leq j \leq N, \tag{9.10}$$

where $\alpha_{\min}$ and $\alpha_{\max}$ are the minimum and maximum values that the pressure boundary condition can be for any electrode. These constraints come from the limitations of varying the contact angle (i.e., contact angle saturation). Hence, $\alpha_{\min}$ and $\alpha_{\max}$ are related to the maximum and minimum contact angles achievable in the EWOD device. In order to satisfy (9.10), we take the solution α to (9.9) and transform each of its components so that the full dynamic range of boundary forcing is utilized (see Fig. 9.10).

With this new transformed α, we know what the pressure boundary values should be to realize the desired pressure gradient field. But it is not possible to exactly enforce α because we cannot directly control the planar curvature term κ in (9.5). For a circular droplet, the planar curvature term is constant and has no effect on the pressure gradient field [76]; hence, it can be ignored. Using (9.5), it is straightforward to compute the contact angles needed to implement α. For noncircular droplets, we still use the same procedure. It is not reasonable to use the planar curvature term in our control algorithm because it involves 2nd derivatives of data that cannot be accurately measured in experiments [77]. Instead, we view it as a small error to the desired directional forcing of the particles. This error grows as the droplet deviates from being a circle. This is not a problem for particle steering for two reasons. First, the linear transformation of the boundary conditions in Fig. 9.10 ensures maximum forcing of the particles. Thus, the relative magnitude of the error
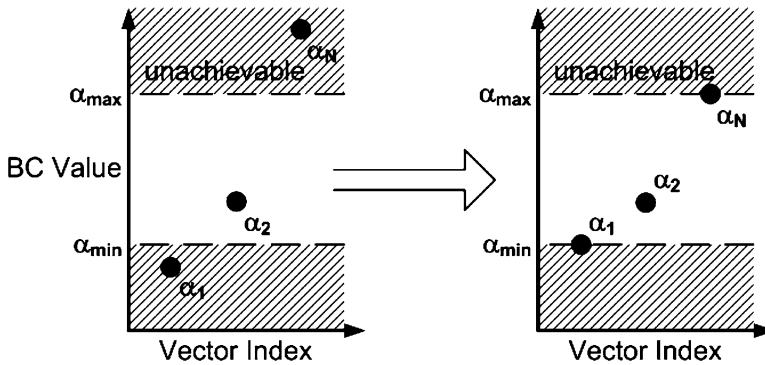
Fig. 9.10 Linear transformation of boundary conditions. An example of satisfying the boundary condition constraints is shown above. On the *left*, the components of the solution to (9.9) are plotted with the maximum and minimum constraint bounds denoted by *dashed lines* (see (9.10)). On the *right*, the components have been linearly mapped to enforce the constraints. This introduces a scaling factor into (9.9), which affects the magnitude of the pressure gradient b vector (i.e., the magnitude of the force acting on the particles). In effect, this causes the particle to be forced as much as possible in the desired direction – it imposes a limit on the maximum velocities that can be applied

due to the *xy* planar curvature is minimized. Second, any particle trajectory tracking errors that may occur are corrected through our feedback system (see the numerical simulations in the next section). However, the planar curvature does limit the type of trajectories that the particles can follow and this is also discussed in the next section.

Finally, the electrode voltages needed to actuate the contact angles corresponding to the pressure boundary vector α are computed by inverting the curve-fitted data of the contact angle versus voltage function $\theta(V)$.

Apply Voltages, Update Particle Position, Advance to the Next Time-Step

Our simulation advances to the next time step after using the voltages computed above to solve for the induced pressure and velocity fields. The velocity field is then used to update the position of the particle (see Fig. 9.11). The scaling described in Fig. 9.10 ensures the particle will be forced as fast as possible along the desired direction. Our algorithm runs by repeating this process for each time step.

Multiple particle steering is easily handled by applying the above discussion to each particle and its respective trajectory. The only change is that the linear system above has more rows to accommodate the extra particles. If the number of electrodes is limited, then this can adversely affect the controllability we have. In a single
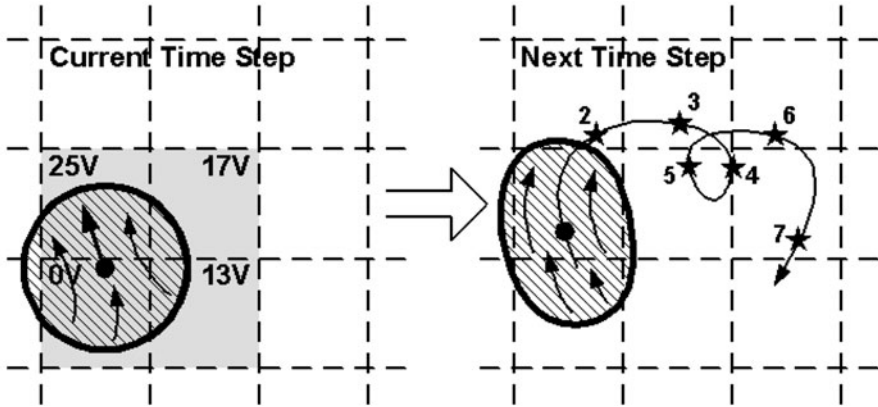
Fig. 9.11 EWOD particle steering control algorithm update. The droplet configuration from Fig. 9.8 is shown in the diagram above. The direction of motion for the particle is toward the trajectory point that is just out of reach for the current time-step. This control strategy ensures the particle will move as fast as possible and stay close to its desired trajectory. On the *left*, the *shaded* electrodes contain the voltages needed to move the particle in the desired direction. These are computed by the least-squares solution discussed above and by the inversion of the contact angle versus voltage curve-fit $\theta(V)$. The varying voltage grid induces a pressure gradient field inside the droplet such that the pressure gradient at the particle is pointing along the desired direction of motion. This moves the droplet and particle along the trajectory to the next time-step

small droplet, a single particle can be made to track interesting trajectories as long as the droplet overlaps enough electrodes (see Figs. 9.12 and 9.13). Also in a small droplet, two particles can be controlled for simple trajectories as shown in Fig. 9.14. For more than two particles in small droplets, all but the simplest trajectories (i.e., straight lines) cannot be tracked. This is a consequence of the number of actuators (N, which is typically around four for small droplets that only touch neighboring electrode pads) needing to exceed the number of particle degrees of freedom ($2m$) for the inverse problem to have an exact solution. For larger droplets that overlay more electrodes, control of more particles should be feasible.

9.2.2.2 Simulation Results and Discussion

In this section, we present some results that demonstrate basic electrowetting particle steering control using our experimentally validated simulations. A 3×3 electrode grid is used to actuate and control the droplet and each square electrode is 1.4 mm on a side. We present four cases that are controllable and three cases that are not and then discuss the possibilities and limits of our method. The voltages generated by our algorithm are reasonable and are within the limits of the UCLA device discussed in [39].
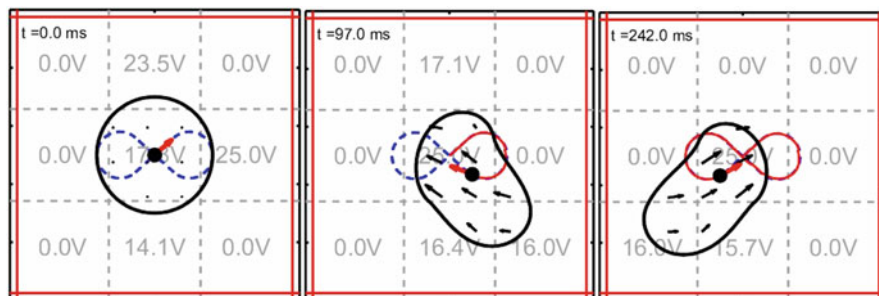
Fig. 9.12 Particle following a figure "8" path. In the simulation results above, we have a droplet (denoted by the *thick black curve*) lying on a 3 × 3 grid of electrodes (denoted by the *dashed lines*). The *blue dashed curve* is the desired figure "8" path and a *black dot* represents the particle with a *thick red arrow* pointing in the desired direction of travel. The *red curve* is the actual path of the particle. The *black arrows* inside the droplet denote the fluid velocity field inside the droplet. The voltages on the grid are time varying in such a way as to keep the particle moving along the path and are computed using the control method above, (9.8)–(9.10) [72]. (Used with permission. Copyright Royal Society of Chemistry)
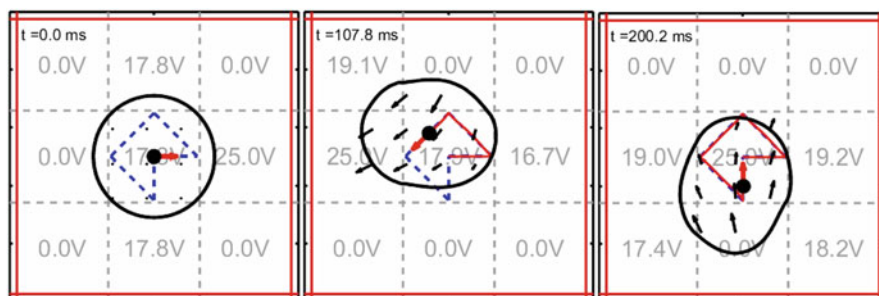
Fig. 9.13 Particle following an angular path (same format as in Fig. 9.12). The particle is able to track the trajectory very well, including at the corners

Controllable Cases

Figure 9.12 shows a droplet moving in a way that makes a particle floating inside follow a figure "8" path. A circular droplet starts on the center electrode with a particle resting in the center of the droplet. The blue dashed curve represents the desired trajectory, which is made up of a fine sampling of points. Two segments are used to represent the trajectory because of the self-intersection. The voltages on the electrode grid are actuated using the control algorithm above, which causes the particle to move forward along the trajectory. For this case, the droplet always overlaps enough electrodes to allow it to be controlled in a way that keeps the particle moving on the figure "8" path. The particle never deviates more than 20 micrometers from its desired trajectory.
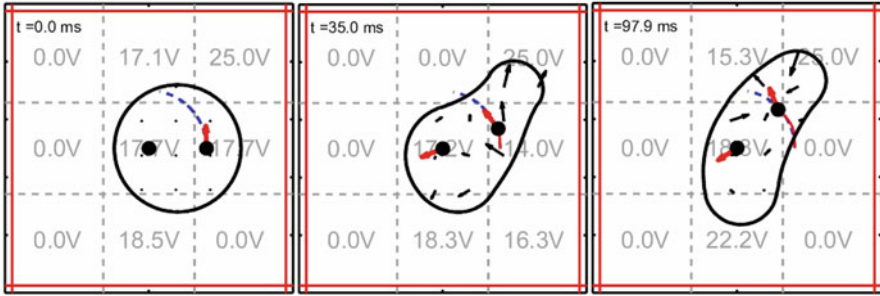
Fig. 9.14 Two-particle control: one particle moves on a quarter circle, the other is stationary (same format as in Fig. 9.12). The stationary particle's trajectory is a single point. As the particle on the right follows the circular arc, the droplet distorts to accommodate both particle motions

In Fig. 9.13, a particle is shown following an angular path that is represented by five separate straight line segments. This is to prevent the particle from rounding off the corners as it travels along the trajectory. Just as in Fig. 9.12, the droplet always overlaps enough electrodes to keep the particle on the path, with a maximum deviation error of 25 μm.

An example of two-particle control is shown in Fig. 9.14. One particle is held stationary while the other moves along a circular arc. The trajectory for the stationary particle consists of a single point, which ensures that it stays close to that point. As the particle on the right follows the circular arc trajectory, the stationary particle oscillates around its desired position to within 10 μm. The droplet itself becomes deformed because of the limited actuators and the restrictive task of moving one particle and holding another still. This also prevents the particle on the circular arc from moving past the point shown in the last frame of Fig. 9.14 and completing the circle.

In Fig. 9.15, we demonstrate particle separation. A droplet starts in the first panel with two particles spaced 0.31 mm apart. Both particles follow separate diverging trajectories designed to stretch the droplet and separate the particles. Once the particles are near the ends of their trajectories (see the third frame), our control algorithm turns off and we command an open-loop voltage of 25 V on the middle left and right electrodes and zero volts everywhere else. This causes the droplet to split into two smaller drops, each of which contains a single particle. The reason for not using our control algorithm to complete the split is because of numerical instability. When both particles are in the lobes of the dumbbell shape of the pinching droplet, the available forcing at the particles' positions is fairly weak. This would cause the condition number of the G matrix in (9.8) to degenerate and produce errors in the least-squares solution. Therefore, we avoid this by commanding open-loop voltages that we know will split the droplet (see Fig. 9.6a). Also, see Fig. 9.17 for an example of how this numerical instability can affect particle control.
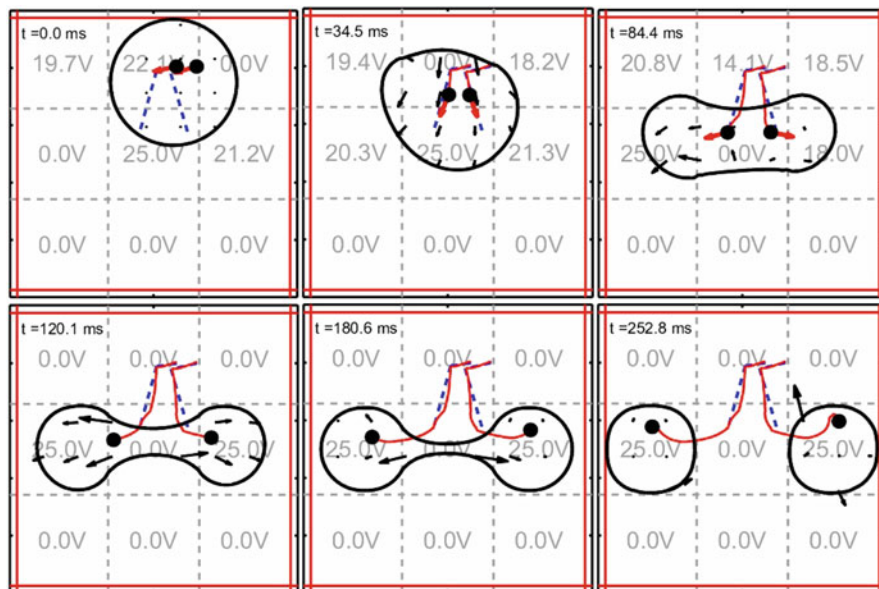
Fig. 9.15 Two-particle separation into two satellite drops (same format as in Fig. 9.12). Each particle first follows a trajectory that takes them away from each other. When there is sufficient distance between the two particles, our control algorithm turns off and the separation is completed in the usual way by applying the open-loop voltages used in the experimental splitting example (Fig. 9.6a) [72]. (Used with permission. Copyright Royal Society of Chemistry)

Uncontrollable Cases

We now show some cases that cannot be effectively controlled. In Fig. 9.16, a particle is shown trying to track a sine wave path. The particle is able to track the trajectory very well until near the end where there is a kink in the particle's path. The loss of tracking is because the droplet's shape and position at that moment are such that the number of available electrodes is very limited. It becomes impossible to create a pressure gradient field that will continue moving the particle in the tangential direction of the desired trajectory. Hence, the particle drifts away from the trajectory by more than $100\,\mu$m. This situation corresponds to (9.9) having no exact solution, which means only a least-squares best fit of the desired pressure gradient can be computed. Eventually, however, the particle is able to reacquire the trajectory.

Figure 9.17 shows two, initially separate, particles trying to come together and touch. The desired motion of the particles induces the droplet to try and pinch together in an effort to have the particles touch. However, when the particles begin to near each other, the droplet ceases its splitting action. Instead, the droplet holds the necking region and begins to oscillate up and down. This is because we are
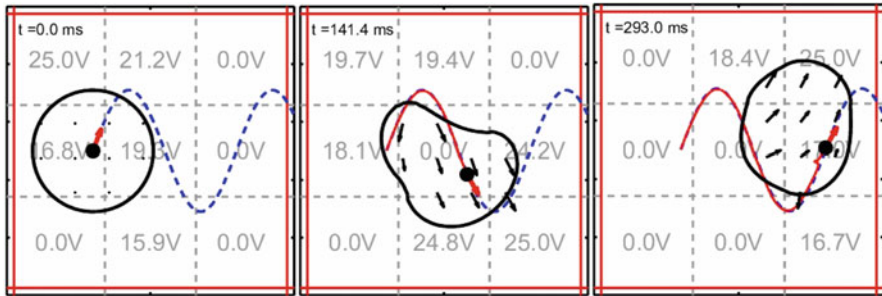
Fig. 9.16 Particle traveling on a sine wave (same format as in Fig. 9.12). The particle is able to track the sine wave path until the last time frame where the particle drifts away from the desired trajectory (see the kink in the particle's path)
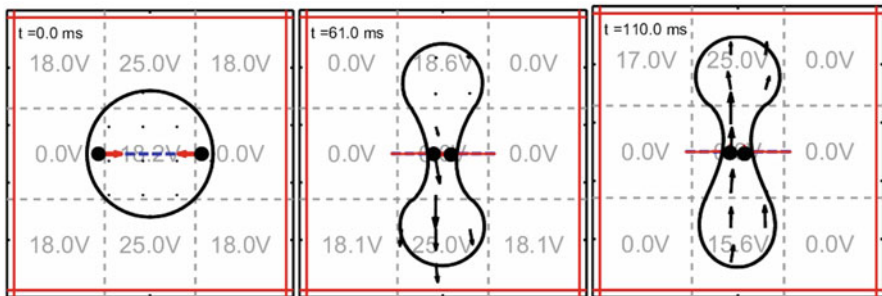
Fig. 9.17 Two particles trying to come together and pinch a droplet (same format as in Fig. 9.12). The particles travel on two separate trajectories that would, ideally, bring them together. However, as they come together, numerical instabilities in (9.9) cause random variations in the control voltages. This causes the droplet to hold its shape and move up and down in an undesirable way

trying to specify two opposite directions of motion at points that are very close together, which leads to a numerical instability in solving (9.9). As the particle positions get closer together, the condition number of the matrix G degenerates causing spurious oscillations in the control voltages. The droplet is unable to bring the particles together, much less pinch, because of the randomly varying electrode voltages.

Figure 9.18 shows two particles trying to follow diverging paths. At first the droplet is able to deform enough to keep the two particles on their respective trajectories but this quickly fails. The droplet is unable to continue deforming in a way that keeps both particles on track and moving forward. Since the trajectories are just straight lines represented by two points each, the control algorithm keeps the particles moving forward while trying to force them toward the endpoints of the trajectories. The end result is both particles stay roughly parallel with each other and are unable to recover their trajectories. This stems from a lack of available electrodes and the limitations imposed by contact angle saturation.
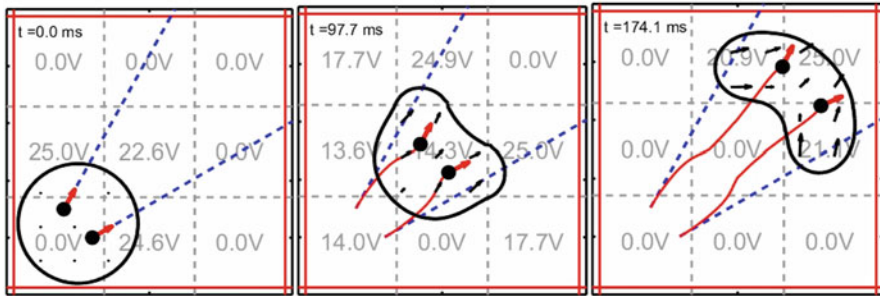
Fig. 9.18 Two particles on diverging paths (same format as in Fig. 9.12). Each particle is attempting to follow separate trajectories, both of which lead away from each other. Due to limitations of the pressure boundary actuation, and a lack of electrodes, the control algorithm is unable to keep both particles moving on their respective paths

The limitations of achievable electrowetting particle control arise from having a small number of electrodes available for actuation and from contact angle saturation. Moving several particles in different directions requires many degrees of freedom in adjusting the pressure boundary conditions. As the droplet moves, it must overlap enough electrodes to allow the realization of the pressure gradient field needed to push the individual particles along their trajectories. Hence, a finer electrode grid would allow more precise control of more particles simultaneously (not surprisingly, it is more challenging to fabricate electrowetting systems with a finer grid of electrodes). Also, some trajectories will require the droplet to become extremely distorted and may require it to split into several pieces. To do this, one needs enough dynamic range in the boundary forcing to overcome the droplets natural tendency to remain in a circular shape (see the *xy* planar curvature term in (9.5)). Contact angle saturation limits the boundary forcing and the degree of droplet deformation, which can cause controllability to be lost and particles to drift off their desired trajectories (see Figs. 9.16 and 9.18). In addition, if two particles are very close together, it is not possible to force them in arbitrary directions. The limits of boundary forcing and the numerical instability that enters into solving (9.9) inhibit close-particle control (as in Fig. 9.17) no matter how many actuators are present.

As of today, EWOD devices employ an electrode pitch and are then used to manipulate droplet of about that size (if the electrodes are made smaller, then smaller droplets can be used). This means that there are only a few actuators per droplet and this allows control of only one or two particles per droplet. Nevertheless, it is both interesting and surprising that existing electrowetting systems already have enough control authority to steer single particles along complex trajectories and to steer two particles along simple paths – usually it is assumed that additional types of control (e.g., laser tweezers, magnetic forces, etc.) are required to control single particles inside EWOD systems. In our next example, which uses electro-osmotic or electrophoretic control, it is possible to control particles with more freedom, to do so to nanometer precision, and to control particles that try to swim away (we control

swimming bacteria). We also have initial results on three-dimensional control and controlling the orientation of objects by creating flows with the right amount of shear at the objects location.

9.3   Manipulating Objects by Flow Control and/or Electrophoresis

As in macroscale technologies and applications, there is a need to put things where they need to go (cells into testing chambers or to sensor locations, quantum dots into photonic cavities), and this is difficult to do on the microscale. We have developed, and experimentally demonstrated, a suite of techniques based on feedback control of the surrounding flow and/or electric fields to steer, place, and hold objects in microfluidic systems. Flow control methods to individually position *and* orient micro- and nanoscale objects, such as nanorods, are being demonstrated next.

Our approach has advantages over laser tweezers and optoelectronic methods [78–81], which are the current state-of-the-art approaches for manipulating micro- and nanoscale objects. Our method is simpler and cheaper. We can control any kind of visible objects in liquid solutions, not only objects with the right dielectric properties to permit force trapping by optical or optoelectric means [82]. Our method can be integrated into a hand-held system, and position error correction is implemented over a large working area instead of relying on particle capture into a small optical trap [83] thus allowing robust manipulation over a large region. And our method has a more favorable scaling with object size [84] – optical forces scale with the volume of the object making it difficult to control very small objects [85], fluid control forces scale with the object diameter [15] so we get bigger forces more easily at the nanoscale. Our large control working region has allowed us to steer and hold swimming bacteria (we continuously bring them back as they try to swim away) and the more favorable force scaling has allowed us to manipulate single quantum dots to nanometer precision for as long as they remain visible [84] without using high power lasers that can damage the particles they are meant to control. Our method also has limitations compared to optical methods: laser tweezers can control more particles at once [82] and they can more readily be used to quantitatively measure particle-to-particle interactions [86, 87] (for us to measure such forces would require precision inversion of a fluid dynamic model that has uncertainties in it that will degrade the inversion). Laser tweezers are also routinely used for three-dimensional manipulation whereas we have only recently demonstrated three-dimensional control in simulations [88].

Current applications for our method include manipulation of cells on chip for basis science biology studies and for lab-on-a-chip applications such as sample preparation (e.g., sorting out cells of interest, such as bacteria, stem cells, or circulating tumor cells, from human samples), and positioning quantum dots on photonic

crystals for creating multidot quantum information systems [89]. We envision being involved in many additional applications now that the method is mature and has been experimentally demonstrated to be flexible, robust, and nanoprecise.

9.3.1 System Setup and Device Fabrication

Our basic system to manipulate micro- and nanoscale objects by flow or electrical control consists of a microfluidic device, a microscope and a camera to observe the location of objects inside the device in real-time, actuating electrodes powered by a digital to analog converter, and a control algorithm on a standard personal computer (Fig. 9.19). The microfluidic device is made out of a soft polymer (polydimethylsiloxane (PDMS)) and is fast and easy to fabricate. It can be laid on top of other devices, e.g., on top of a glass device with patterned chemical features, on top of a silicon device with other MEMS capabilities, or on top of a photonic crystal for our quantum dot placement project. Details on system setup are given in [83]. More advanced capabilities, to manipulate swimming cells, to steer and trap multiple particles at once, and to place single quantum dots to nanometer precision on chip are described in [83, 84, 89].

9.3.2 Physics and Modeling

Our system can actuate micro- and nanoscale objects in one of two ways. It can either move the fluid in the device by electro-osmotic actuation (described next) to carry particles along, this works for both neutral and charged particles; or, if a particle is charged, then it can be actuated by an electric field which applies an electrostatic (Coulomb) force and moves the particle relative to the surrounding fluid (electrophoretic actuation) [49, 50]. Particles often acquire a surface charge through weak chemical interactions with the surrounding fluid, for example the polystyrene beads we used in [83] have a surface charge in water as do the yeast cells we also controlled. Thus charged particles are the norm rather than the exception but the amount of charge can vary depending on the chemistry of the object and the surrounding medium.

Electro-osmotic actuation of flow is routine in microfluidic devices, e.g. [90–92]. Here an applied electric field electrophoretically moves a thin layer of charges that form naturally at the fluid/device interface. Typically, these charges are ions present in the liquid that migrate to the solid/liquid boundary to shield stationary charges formed there, for example, by weak acid/base chemistry occurring at the interface (the same type of chemical mechanisms also lead to charge formation on the surfaces of particles). Which charges (positive or negative) and how much they accumulate inside the liquid immediately adjacent to the device surfaces depends on the chemistry of the liquid and solid materials, on the pH, the amount and type of dissolved ions, surface treatments, and many other factors [93–95]. The electric

Electrode	Signal name	DAC pin
1	VOUT0	1
2	VOUT1	29
3	VOUT2	3
4	VOUT3	31
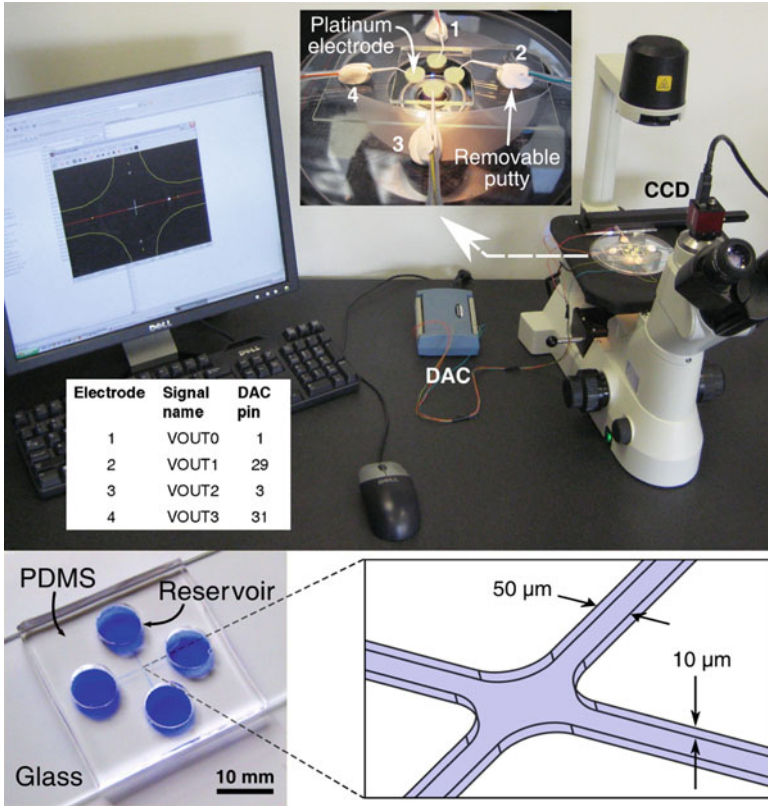
Fig. 9.19 Our flow control system for a single particle. *Top*: Photograph of the experimental setup, the flow control device is on the right on top of the inverted microscope which is connected to a CCD camera. *Bottom left*: Photograph of a four-channel PDMS on a glass device filled with blue food coloring to clearly show the microfluidic channels and reservoirs. Each microchannel is 10 mm long, 50 μm wide close to the particle steering intersection region and 300 μm wide otherwise, and 10 μm deep. *Bottom right*: Schematic of the channel intersection and the 100 μm × 100 μm cell steering control area. The corresponding system closed-loop block diagram is shown in Fig. 9.21

field applied by the electrodes moves these free charges (the Debye layer) in one predominant direction. This thin moving layer of charges then drags the rest of the fluid along by viscous forces, the electro-osmotic actuation (Fig. 9.20). (Charges in the interior of the fluid do not cause a net fluid motion, since there is essentially an equal number of positive and negative ions. Only a small fraction of ions of one type are taken away into the Debye layer. The remaining interior charges create equal and opposite electrical forces on the fluid in the channel center, their only net effect is to move through the fluid and heat it.) A more detailed description and analysis of the physics of electro-osmotic actuation can be found in [49, 50, 96].
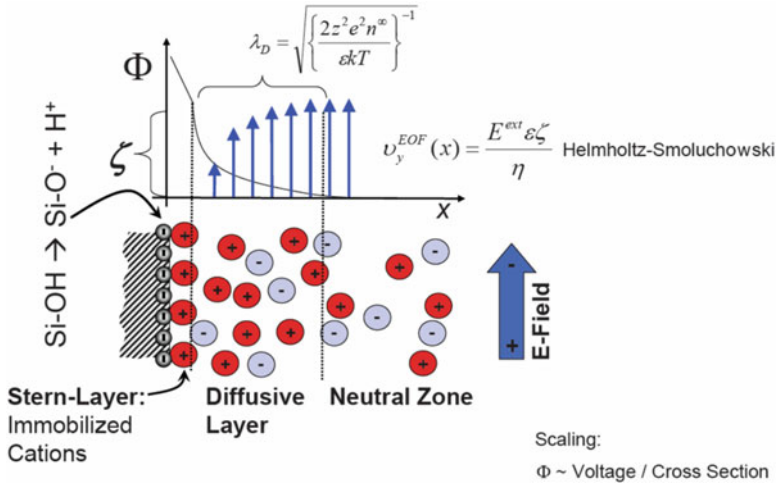
Fig. 9.20 The physics of electro-osmotic actuation. A schematic side view through a microfluidic channel is shown (the channel wall is on the left side, the flow is being electro-osmotically actuated up the channel by the applied electric field). The *minus* signs represent the fixed charges at the solid/liquid interface, *large circles* (+ or −) show ions naturally found in the liquid (e.g., in water). These ions accumulate to shield the surface charges forming a thin Debye layer that has a predominant charge (here mostly positive, on the left). The electric field moves this layer and it drags the fluid in the channel by viscous forces. Charges in the interior of the channel (the "neutral zone") remain essentially balanced (only a small fraction of the charge goes to the surfaces) and so they create no net fluid motion effect [96]. (Used with permission. Copyright COMSOL)

In electro-osmotic flow the fluid is dragged by moving charges that are actuated by the applied electric field. In our planar devices this means that the flow will follow the electric field that is present at the floor and ceiling of the device. The electric field we apply is uniform in the vertical direction but it can have complex patterns in the horizontal xy plane. The resulting microflow will exhibit these same complex horizontal patterns. It is possible to show this rigorously starting from the Navier–Stokes equations, as we do in [97], the end result is that the fluid velocity follows the applied electric field essentially instantaneously (with a microsecond time constant) [98, 99]. Thus, see also [49],

$$\vec{V}(x,y,z,t) = (\varepsilon \xi / \eta)\, \vec{E}(x,y,t) = -(\varepsilon \xi / \eta)\nabla \phi(x,y,t), \qquad (9.11)$$

where $\vec{V}$ is the electro-osmotic fluid velocity, $\vec{E}$ is the applied electric field which is uniform in the vertical direction, ϕ is the electric potential as created by the actuators of Fig. 9.19, ε is the permittivity of the liquid, η is its dynamic viscosity, and ξ is the zeta potential (essentially the voltage) at the liquid/solid interface [49, 50]. Electric fields are governed by Laplace's equation, the electrostatic limit of Maxwell's equations [51], with boundary conditions at the electrodes set by the voltages that we apply there.

In the above it is ξ which quantifies the amount of charge that is contained in the Debye layer. Since this value depends on the details of the surface chemistry and cannot be predicted a priori, it is usually inferred from experiments by applying a known electric field and measuring the resulting flow velocity. The chemistry that happens at the solid/liquid interface is complicated and so the above discussion of electro-osmotic actuation should be understood as a first order simplified explanation (further explanations can be found in [100, 101]). Although the underlying chemical principles of electro-osmosis are still not well understood, that does not prevent us from using it to precisely control microscopic and nanoscopic particles as we show in the remainder of this chapter.

Neutral particles are carried along by the created electro-osmotic flow. In addition, these particles experience Brownian motion. When the particles are comparable in size to the channel height, as for example the yeast cells that are $\sim$5 µm in diameter compared to the 11 µm high channels we used in [83], then the channel floor and ceiling constrain vertical diffusion. When the particles are small, e.g., the nanoscopic quantum dots, then they diffuse in all three directions. In either case, we only control their motion in the xy plane leaving their motion to be free in the z-direction.

Thus, in the plane, the particle positions are governed by $\dot{\vec{P}}_j = \vec{V}(\vec{P}_j) + \vec{w}$, where $\vec{w}$ is Brownian noise and $\vec{P}$ is the vector of particle x and y positions. The electric potential is described by Laplace's equation $\nabla^2 \phi = 0$ with Dirichlet boundary conditions at the electrode boundaries $\phi(\partial D_j) = u_j$, where ∂D_j denotes the liquid/electrode interface location and u_j is the jth applied voltage. Insulating Neumann conditions hold at other surfaces. The solution of Laplace's equation is linear in the applied voltages so:

$$\dot{\vec{P}} = \vec{V}\left(\vec{P}\right) + \vec{w} = c\vec{E}\left(\vec{P}\right) + \vec{w} = -c\nabla\phi\left(\vec{P}\right) + \vec{w} = -c\sum_{j=1}^{n}\nabla\phi_j\left(\vec{P}\right)u_j + \vec{w},$$
(9.12)

where $c = \varepsilon\xi/\eta$ is the electro-osmotic mobility, ϕ_j is the solution to Laplace's equation when electrode j has a unit applied voltage and all other electrodes are at zero voltage, and $\vec{u}$ is the time-varying vector of applied voltages. Note that the velocities of the particles are in the direction of the locally applied electric field and so depend on where they are with respect to the electric potential $\phi(x, y)$. For the same set of voltages, two different particles in two different locations can be actuated in different directions. In summary, the equations to be controlled for m neutral particles are linear in the control and nonlinear in the particle positions, they are:

$$\dot{\vec{P}} = A\left(\vec{P}\right)\vec{u} + \vec{w},$$
(9.13)

where $\vec{P} = (x_1, y_1, x_2, y_2, ..., x_m, y_m)$ is the position vector for the planar location of the m particles of interest and the A matrix contains spatial information about the electric fields originating from each electrode.

If the particles are charged then there is an added electrostatic force that also points with the electric field – either along it for a positively charged particle or directly opposite it for a negatively charged particle. This can be incorporated into the *A* matrix by modifying the mobility coefficient for each particle. Variations in the electro-osmotic zeta potential and the amount of charge on the particles can change these mobility coefficients, but the control algorithm is robust to these variations – the control basically sets the direction of particle motion at the location of each particle. So long as the sign of the mobility coefficient for that particle does not flip (a rare occurrence) the control works. To further improve performance, we usually identify the mobilities of the particles of interest before starting an experiment by applying a known electric field and observing their resulting velocity through our vision system. Our particle steering experiments in [83] function to 1 μm precision even though the polystyrene particle and cell mobilities in that case are only known to within ±50%. Our quantum dot experiments show 45 nm accuracy even though the charge on the QD also varies.

9.3.3 Feedback Control

Figure 9.21 shows the basic control idea for a single particle: a four channel microfluidic device, an optical observation system, and a computer with a control algorithm are connected in a feedback loop. The vision system locates the position of the particle in real-time, the computer then compares the current position of the particle with the desired (preprogrammed or user input) particle position, the control algorithm computes the necessary actuator voltages that will create the electric field, or the fluid flow, that will carry the particle from where it is to where it should be, and these voltages are applied at electrodes in the microfluidic device. For example, if the particle is currently South/East of its desired location, then a North/West flow is created. The process repeats at each time instant and forces the particle to follow the desired path (see [83, 102] for details).

Surprisingly, it is also possible to steer multiple particles independently using microflow control [20]. A multielectrode device is able to actuate multiple fluid flow or electric field modes. Different modes cause particles in different locations to move in different directions. By judiciously combining these modes, it is possible to move all the particles in the desired directions. We note here that this kind of flow control, where we control the fluid so precisely that we can hold or steer multiple objects at once in different locations, is not possible in macroscale fluid dynamics. Here we are exploiting the linear nature of the electrostatic equations and Stokes flow (the nonlinear fluid momentum terms, the "Navier" part, are negligible on the microscale) to be able to invert the problem to achieve control. We certainly would not be able to invert a high Reynolds number or turbulent flow in the same fashion since it would amplify small changes in actuation to large errors in particle motion.

The multiparticle steering control algorithm is more sophisticated than the single-particle algorithm: its operation relies on inversion of the flow and electric fields
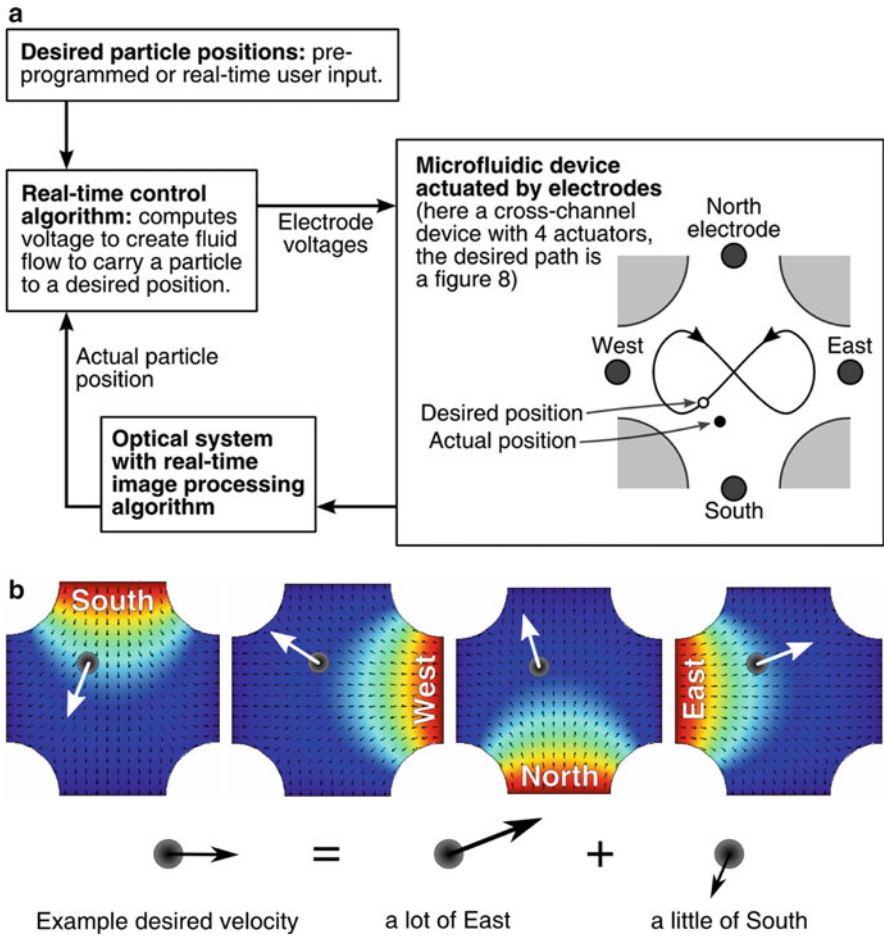
Fig. 9.21 (**a**) Feedback control steering approach for a single particle. A microfluidic device with electro-osmotic actuation is observed by a vision system that informs the control algorithm of the current particle position. The control algorithm compares the actual position against the desired position and finds the actuator voltages that will create a fluid flow, at the particle location, to steer that particle from where it is to where it should be. The process repeats continuously to steer the particle along its desired path. (**b**) Four basic flows that can be generated by applying a voltage to each electrode individually (from simulations). By actuating these four flows together correctly, it is possible to generate an electrokinetic (electro-osmotic + electrophoretic) velocity at the chosen particles location in any desired direction to always carry that particle from where it is to closer to where it should be [83]. (Used with permission. Copyright IEEE)

predicted by the model. An eight-electrode device, as in Fig. 9.22, can create seven independent electric/fluid modes (one of the eight electrodes acts as ground, or, equivalently, if the electrodes float, raising or lowering all of them by a constant voltage does not impact the electric field, so only seven degrees of freedom remain).
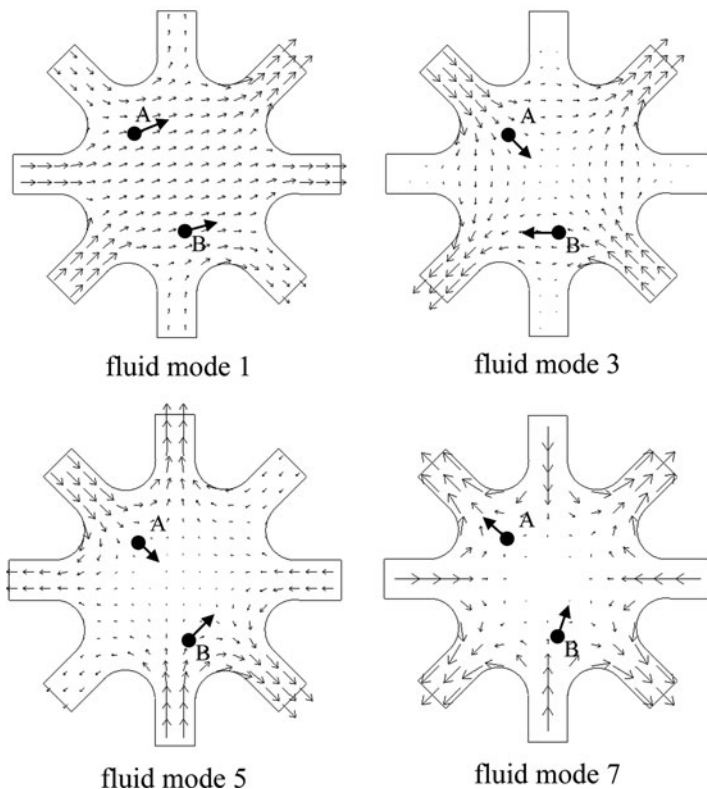
Fig. 9.22 Electro-osmotic microflow modes for an eight-electrode device. The above figure shows the first, third, fifth, and seventh modes computed from the model stated above (also see [20, 83]). The two example neutral particles A and B (shown as *black dots* above) will then experience the velocities shown by the *arrows* [83]. (Used with permission. Copyright IEEE)

Four of these seven modes are shown above. The key point is that the different modes force particles at different locations in different directions (see particles A and B in Fig. 9.22): by intelligently actuating a combination of modes, we can force all the particles toward the right locations at each instant in time. Since each particle has two degrees of freedom (an x and a y position), an eight-electrode device can precisely control up to three particles (particle degrees of freedom $3 \times 2 = 6 \le 7$ actuation degrees of freedom).

In its simplest incarnation, the multiparticle control algorithm works as follows (details in [20]). We define a desired correction velocity vector between where all the particles of interest are observed to be versus where we would like them to be at the current time:

$$\vec{v}_{\text{correction}} = k\left(\vec{P}_{\text{desired}} - \vec{P}_{\text{observed}}\right), \tag{9.14}$$

here k is the control gain. Our task is now to choose the voltages at the electrodes to create a velocity as close to this desired correction velocity as possible. Since, by (9.13), there is a linear relation between the control and the velocity (we know the particle positions since the camera can see them), and since this velocity is achieved essentially instantaneously as soon as we apply the voltages, we can solve a static linear problem to determine the needed set of electrode voltages. Specifically, as in the EWOD problem, we solve a least-squares problem to find the set of actuator voltages that will create velocities at all the particles of interest as close as possible to the desired correction velocities. The other particles (the particles not of interest) are actuated in some random way that depends on the electric fields they will see at their locations. This gives the feedback control:

$$\vec{u}^* = \left[A^T \left(\vec{P} \right) A \left(\vec{P} \right) \right]^{-1} A^T \left(\vec{P} \right) \vec{v}_{\text{correction}}$$

$$= k \left[A^T \left(\vec{P} \right) A \left(\vec{P} \right) \right]^{-1} A^T \left(\vec{P} \right) \left(\vec{P}_{\text{desired}} - \vec{P}_{\text{observed}} \right). \quad (9.15)$$

For the case where there are more actuation than particle degrees of freedom ($n - 1 \geq 2m$), the A matrix typically has full row rank (unless two particles are at the same location) and the above least-squares answer achieves the desired velocity with minimum control effort (with minimum $\|\vec{u}\|_2$) [75]. For cases where we try to control more particle degrees of freedom than we have actuators, the experimental performance rapidly degrades to unusable. For example, four particles (eight degrees of freedom) can be controlled badly by eight electrodes (seven degrees of freedom, one electrode is ground), but five particles cannot. Since it is possible to fabricate devices with many electrodes, the real limit to the number of particles that can be controlled is the condition number of the matrix A as discussed below.

We pre-compute the electric fields that make up the matrix A ahead of time, this means we can use a lookup table to determine A for any particle positions $\vec{P}$ seen by the camera. We then compute the pseudo-inverse $(A^T A)^{-1} A^T$ in real-time, in milliseconds, as the control proceeds. It is convenient to carry out this calculation in the coordinate system of the fluid modes of Fig. 9.22 (the singular values modes of the matrix A evaluated on a fine grid of points). The dominant (lower spatial frequency) modes are the ones that are better conditioned: at the higher spatial modes very high voltages are required to create even small fluid velocities. Thus we truncate our matrix A onto these first modes and compute the pseudo-inverse above for that well conditioned matrix. It is in fact this conditioning that sets how many particles we can control at once. For our experimental image sensing and actuation errors, we can robustly access just over the first ten or so modes which means we have been able to control up to five particles simultaneously in experiments. There are also other issues, such as a limit to the voltage that can be applied at the electrodes. Too high a voltage causes electrolysis [103], a chemical reaction that creates bubbles, and must be avoided – this voltage limit depends

on buffer and electrode chemistry, for us it is around 10 V. We have treated this actuation limit in two ways: either by turning down the control gain per particle as we approach this limit or, more rigorously, by phrasing a linear programming constrained optimization to choose the gain per particle to maximize performance but not exceed actuator limits. These two approaches both work equally well in experiments.

Our control works robustly across the entire control region – so long as we have done the singular value mode conditioning above there are no regions or combinations of particle locations where we cannot reliably pseudo-invert A. The only time the inversion fails is if two particles are right on top of each other but we are trying to move them in different directions (this is physically impossible since we have to create two different fluid flow directions at the same location). Indeed, our particles can be controlled very close together – in experiments we have shown an ability to steer particles to within 8 µm of each other.

9.3.4 Experimental Results

9.3.4.1 Control of Single Particles to Micrometer Precision

Experimental results for manipulation of one particle, first reported in [102], needed only a simple control algorithms (if the particle was North/West of its target, we created a South/East flow in the entire device) but required solution of practical issues such as device fabrication, fast and reliable vision sensing, operating in a regime of reliable electro-osmotic actuation but with no unwanted chemical reactions (no electrolysis), and prevention of device fouling and particle sticking. Smoothing out of the control algorithms and optimization of the vision system enabled us to control single particles, e.g., polystyrene beads and yeast cells, to single micrometer accuracy (Fig. 9.23). The achieved single micrometer resolution was set by the 1 µm field of view that corresponded to each camera pixel – so we controlled as well as we could see, to single pixel accuracy. One micrometer also roughly corresponds to a more fundamental vision sensing limit, the wavelength of visible light, which sets the absolute minimum on how close two features can be before they can no longer be distinguished one from the other. We discuss how it is possible to bypass this sensing limit for particle control in the section on controlling single quantum dots to nanometer precision.

9.3.4.2 Control of Multiple Particles to Micrometer Precision

Control of more than one particle at the same time requires the more sophisticated pseudo-inverse control algorithm described previously. Below we show results for steering three particles at once using eight electrodes, all to 1 µm accuracy (again
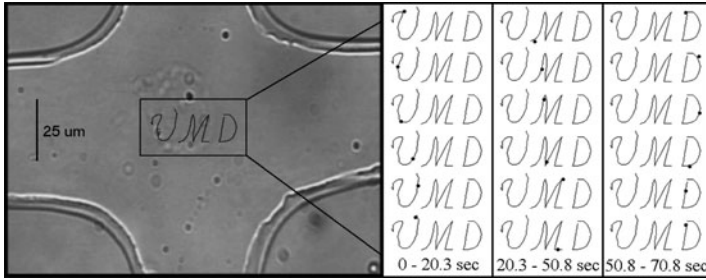
Fig. 9.23 Steering of a slightly charged yeast cell along a UMD path. The cell had an approximate electrophoretic mobility of $c_{ep} = (-23.3 \pm 6.9) \times 10^{-9} \mathrm{m}^2\mathrm{V}^{-1}\mathrm{s}^{-1}$. By comparison, the electro-osmotic mobility of our PDMS devices was $c_{eo} = (36.5 \pm 3.6) \times 10^{-9} \mathrm{m}^2 V^{-1} s^{-1}$. *Left*: Close-up photograph of the microfluidic devices with the desired cursive "UMD" path overlaid on the image. *Right*: The actual path of the chosen 5 μm yeast cell (Red Star® Yeast) (*black dot*) in the feedback control experiment. Snapshots are shown at six equally spaced times for each letter. The yeast cell follows the required trajectory to within 1 μm [83]. (Used with permission. Copyright IEEE)

Fig. 9.24 Steering of two fluorescent beads (2.2 μm diameter, Duke Scientific) around two circles while a third bead is held stationary. In the experiment, the fluorescent beads appear as *small green dots* on a black background and the device geometry, which does not fluoresce, is not visible. Here, the *white dots* are the beads (enlarged), the *solid curves* are the actual trajectories that the target beads have traced out (overlaid), and the *dashed white curves* (also overlaid) show the geometry of the channels and the particle control chamber. Snapshots are shown at three time-steps. The two beads are being steered to within an accuracy of one pixel (corresponding to less than 1 μm). The desired paths are not shown because, at this image resolution, they would perfectly underlay the actual paths. The trapped bead is marked by an *arrow*, and is trapped by the control algorithm to an accuracy of better than 1 μm. Every time the bead deviates from its desired position, a flow is created that pushes the bead back toward its desired location [83]. (Used with permission. Copyright IEEE)

from [83]). We have also demonstrated control of five particles at once but the accuracy is degraded away from 1 μm. This level of control, that it is possible to actuate multiple objects at once in the interior by actuating a fluid by electrodes on its boundary, was and is surprising to the microfluidics community. It is a concrete example, experimentally demonstrated, that shows control theory can enable simple microfluidic systems to perform complex and precise tasks (Figs. 9.24 and 9.25).
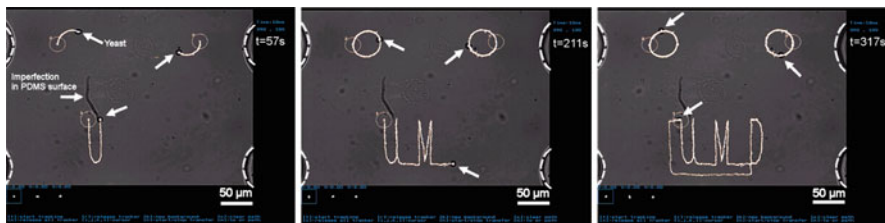
Fig. 9.25 Steering of three yeast cells (5 μm diameter) with small surface charge (electrophoretic mobility $c_{ep} = (-23.3 \pm 6.9) \times 10^{-9} \mathrm{m}^2 \mathrm{V}^{-1}\mathrm{s}^{-1}$) around two circles and a "UMD" path. The cells do not fluoresce. In these images there is no high-pass filter before the camera and the raw images are shown. The yeast cells are visible as small *black dots with a white center* (the three target cells are marked with a *white arrow* in each image), and the *white curves* are the trajectories that the target cells have traced out. The three cells are being steered to within an accuracy of one pixel (corresponding to less than 1 μm) [83]. (Used with permission. Copyright IEEE)

9.3.4.3 Control of Live Swimming Cells

Compared to laser tweezers and optoelectronic techniques [78–81], our technique has the big advantage that it works over a large control area (as shown in Fig. 9.26). This means it is easier for us to manipulate swimming cells: every time they swim away we bring them back (as opposed to moveable trap methods where the bacteria may exceed the optical forces, swim out of the optical trap, and thus escape its intended manipulation). So long as our control can correct the location of the microbe faster than that microbe can swim away it will be effective in trapping and steering it. Whether this can be done or not depends on both the swim speed of the microbe and its preferred swim patterns – fast swimming microbes that like to swim in small circles can be controlled because, even though they swim fast, they do not swim far away; in contrast, medium speed microbes that swim out in straight lines in random directions get further away and are harder to bring back. Below we show initial results for manipulation of medium speed (<10 μm/s) swimmers (Fig. 9.27). We plan to improve our slow control update (every 1/30th of a second) to 300 Hz, this should allow us to control even fast swimmers.

The target applications here involve preparation of biological samples that contain moving organisms, e.g., precisely removing motile bacteria from human samples, steering them to chambers for sensing and subsequent analysis, and (when we achieve control of multiple swimming organisms at once) testing the reaction of one swimming organism against another. Faster hardware (currently we operate at a slow 30 Hz) will allow us to control more often per second and will thus give the microbe less time to escape between control corrections. We also plan to develop smarter control algorithms that will detect and exploit the properties of the specific microbe we are trying to control.
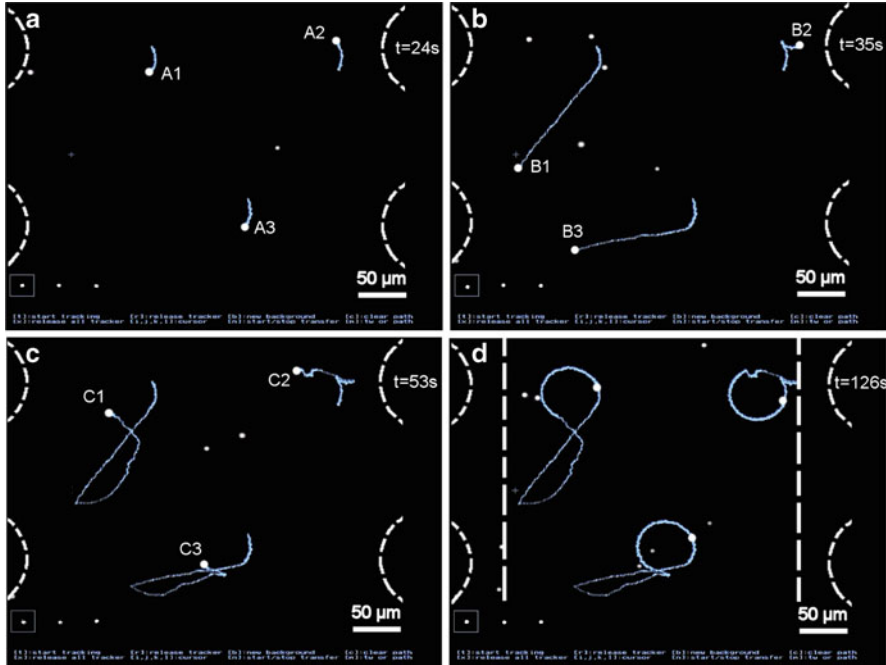
Fig. 9.26 The control algorithm is globally stable and can correct for large errors in particle positions. This figure shows steering of three fluorescent beads ($2.2\,\mu$m diameter, Duke Scientific) around three circles. At time $t = 24$ s, corresponding to bead positions marked A_1, A_2, and A_3, the control was turned off for 11 s, allowing the particles to drift away (primarily due to the slow parasitic flow inside the device caused by surface tension forces at the reservoirs) by up to $150\,\mu$m. The control was then turned back on at $t = 35$ s (B_1, B_2, and B_3), and the control algorithm steered the three original beads back to their desired positions (C_1, C_2, and C_3). Four time instants are shown: (**a**) right before control is turned off, (**b**) right before control is turned back on (the three beads have drifted away a large distance), then (**c**) at a time when the beads are back on track, and (**d**) the final time when the beads have completed the remainder of their three circular paths (again to an accuracy of better than $1\,\mu$m). The two straight lines in the last image illustrate the left and right boundaries of the control region [83]. (Used with permission. Copyright IEEE)

9.3.4.4   Control of Single Quantum Dots to Nanometer Precision

We end this experimental section by showing manipulation of a single nanoscopic particle, a quantum dot, to nanometer precision by flow control. This is needed for creating nanophotonic and nanoelectronic devices, in that situation there is a need to place multiple quantum dots in the high electric field regions of nanophotonic [104–106] and plasmonic [107, 108] structures and this has not been done in any other way. The high field regions of photonic cavities are small, approximately 250 nm in size, so nanometer placement is necessary [109]. (Once one dot has been placed, it is possible to fix it in place by a chemical binding reaction to the surface [110] or
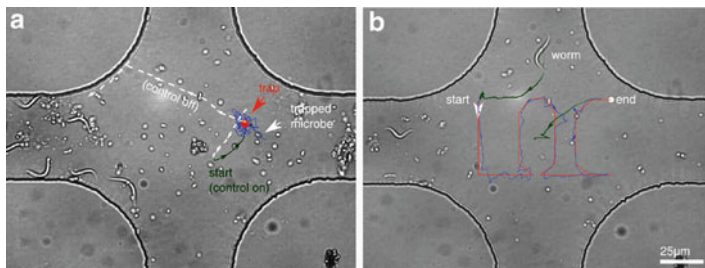
Fig. 9.27 (**a**) A swimming microbe found in river water was moved to an arbitrary trapping location and trapped for 30 s until being released from control. Uncontrolled swimming is shown by a *dashed line*, initial control to the trap or path is shown by a *thin line with arrow heads*, and the controlled motion is shown by a thin line without arrow heads – as is evident, the microbe swims away after the control is turned off which means it was not harmed by the control. (**b**) A worm was steered around a trajectory spelling "LOC" (for lab-on-a-chip)

by solidifying the surrounding fluid [111, 112], thus allowing placement and fixing of one QD after another to make multidot devices.)

In the experimental results reported earlier, our vision sensing accuracy had limited the control precision. That limit was both experimental setup specific (camera pixel size) and more fundamental (the wavelength of light limitation). It is possible to improve the sensing to determine the location of a particle to well below the wavelength of light, in real-time. The key is to realize that a nanoscopic particle, such as a quantum dot, appears as a diffraction limited spot under a microscope, and this spot spans many pixels (see the inset in Fig. 9.29a). By averaging correctly over the many pixels it is possible to infer the center of the diffraction pattern to better than single pixel resolution, a technique known as subpixel averaging [113], which we perform in real-time.

The errors in quantum dot placement are now a combination of vision sensing errors (which can be driven down to tens of nanometers) and diffusion between control updates (which can be reduced by doing control updates more often and by using a higher viscosity fluid – we added a polymer to water that increases its viscosity). Quantum dots also presented other problems that had to be solved to achieve nanometer precision. QDs blink on and off: they blink in and out of view. We pause our control actuation when a QD blinks off and continue actuating when it blinks back on. The QD position is controlled in the horizontal plane but the QD still diffuses in the vertical direction. This diffusion makes the QD leave the focal plane of the microscope and causes a defocusing which hurts our sensing accuracy. Thus we wrapped in a second control loop that uses the variance of the QD image as its metric and drives this metric to a minimum by moving the microfluidic device up or down using a piezo stage. The problem is that going up out of the focal plane and going down below it both look the same, so for this second control loop we introduce a small jitter and then check if the dot looks more focused when going
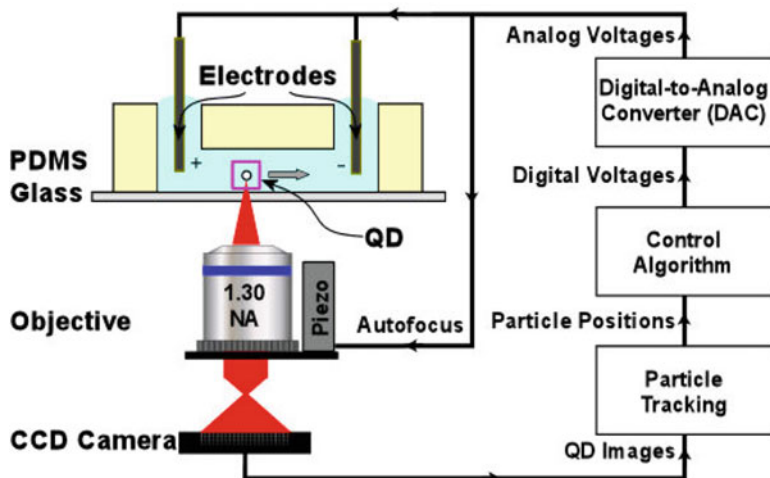
Fig. 9.28 Illustration of the optical and electronic setup for tracking and feedback control of QDs. A CCD camera images the QD and sends the information to a tracking algorithm that uses subpixel averaging to accurately determine the current position of the QD. The control algorithm uses this information to determine the proper voltages to apply to the electrodes in order to move the QD to its desired position. A second feedback loop moves the imaging objective in the *z*-direction using a piezo stage to keep the QD in focus [84,89]. (Used with permission. Copyright American Chemical Society.)

up or down. This tells us if we are above or below the focal plane and we then use a Newton-bracketing algorithm to steer to the minimum image variance. This inner loop runs slowly compared to the main *xy* control loop. The end result is higher accuracy control in the *xy* plane. The vertical loop also tells us where the QD is with respect to the bottom photonic crystal so we can wait until the QD diffuses to the bottom to freeze it in place. Chemistry is also an issue. We had to create a fluid that could be actuated by electro-osmosis, that had a high viscosity, and that was compatible with our device (with PDMS) and with the QDs (would not cause them to fall out of solution). With our colleagues, we are now further creating fluids that satisfy all of the above criteria and, in addition, can be solidified to nanometer precision (by two-photon absorption) [114] to allow us to fix a QD at a photonic crystal cavity by solidifying just a small amount of fluid around it.

Our current single QD positioning results are reported in [84, 89] which includes all details on the experimental setup (Fig. 9.28), the error analysis, and an optical autocorrelation measurement that proves we are indeed controlling just one single quantum dot. We were able to hold a QD at a single location to 45 nm accuracy and steer it along a path with an average deviation of 120 nm (Fig. 9.29). The dot was controlled for 1 hour, its useable (i.e., visible) lifetime.
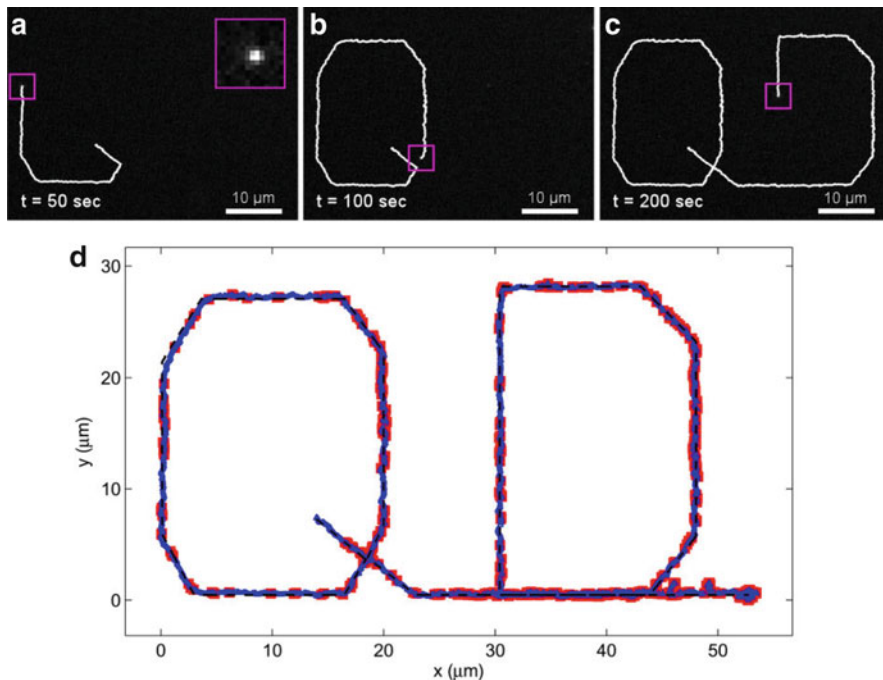
Fig. 9.29 Single quantum dot trajectory. (**a–c**) Time stamped CCD camera images of a single quantum dot being steered along the desired trajectory. The *white trace* shows the measured path of the quantum dot up until its current location. The *square magenta box* shows the subpixel averaging window used to determine the current position of the QD. The *inset* in panel (**a**) shows a closeup of the subpixel averaging window which contains the QD near its center. (**d**) Plot of quantum dot position along its trajectory. The *dotted black line* shows the desired trajectory programmed into the controller. The actual measured QD trajectory is shown in blue. The *solid red squares* depict when the quantum dot blinks off. At the end of the trajectory the QD is held in place for 2 min. The deviation of the QD from the desired trajectory was measured to be 104 nm [84]. (Used with permission. Copyright American Chemical Society.)

9.3.5 Ongoing Research: Toward Three-Dimensional Control and Control of Object Orientation

Control in the third dimension is also possible [88]. A microfluidic device with multiple levels (as shown in Fig. 9.30) can create fluid flows or electric fields with up and down components, in addition to the prior horizontal actuation directions. For example, an actuation from the top North electrode to the bottom South-West electrode will create both a Southwards flow as well as a downward component. As before, different actuation modes move different particles in different directions, and using the same least-squares control algorithm as before these modes can be judiciously combined to create particles velocities as close as possible to desired three-dimensional velocity vectors.
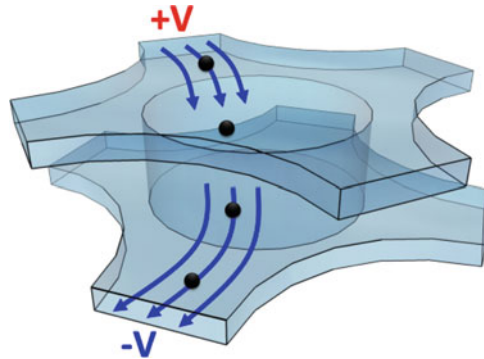
Fig. 9.30 Sample device design for three-dimensional particle control. By placing electrodes in a top and bottom layer, a flow or electric field actuation component can be created from top to bottom or vice versa in the central control region [88]. (Used with permission. Copyright Institute of Physics (IOP) Publishing.)

The device above with eight electrodes can readily control one and two particles in all three dimensions (Fig. 9.31). As previously [83], effective control remains possible in the presence of noise and is still accurate even if the properties of the particles (and the device) are not known perfectly. Control of two 10 nm diameter particles (whose Brownian motion is significant in water) is shown in Fig. 9.32 along two orthogonal and self-intersecting circles. In this case we assumed that the control algorithm does not accurately know the charge on these particles – it believes their charge is $\pm 50\%$ of the true value. In this uncertain case, the simulation shows that manipulation can be achieved with a precision of $2\,\mu$m.

In addition to controlling the position of objects, it is also possible to control their orientation. The discussion below is stated back in two spatial dimensions, but the same method can be used in three dimensions as well. The idea is that now, in addition to creating a translating flow, a flow shear is also created to turn the object. Understanding how to create the right flow is subtle. It is not possible to create a flow rotation: the flow follows the applied electric field and the electric field is irrotational ($\nabla \times \vec{E} = \nabla \times (-\nabla \phi) = 0$).

It is, however, possible to create irrotational flows with shear. Only some types of shear flows can be made. It is not possible to only create the shear flow in one direction as shown in the first panel of Fig. 9.33. The illustrated $\partial u/\partial y$ horizontal flow shear (clockwise rotation) must be exactly cancelled by an equal and opposite vertical flow shear $\partial v/\partial x = \partial u/\partial y$ (counterclockwise rotation) as follows immediately from the zero curl equation for the electric field, or equivalently fluid velocity vector field, $\nabla \times \vec{E} = \nabla \times \vec{V} = \partial v/\partial x - \partial u/\partial y = 0$. But it is possible to create saddle flows, with two balancing shears in opposite directions, as shown in the second and third panels.

If this saddle flow is chosen correctly with respect to the object – here if the shear that will rotate the ellipsoid clockwise is oriented to work on its long axis
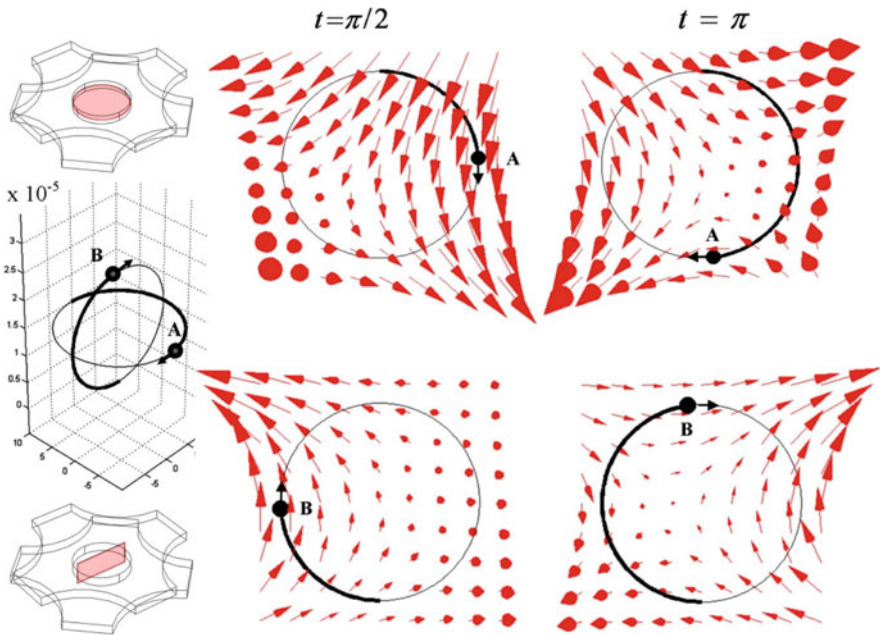
Fig. 9.31 Two charged particles controlled simultaneously on two orthogonal circular paths. The horizontal and vertical paths are shown at the *top* and the *bottom* of the figure, respectively. The desired path of the two particles (*A* and *B*) is in *thin black* and the achieved path is in *thick black*. The (*red*) *arrows* show the created electric field at the two time instants (arrows that appear as *round dots* show flow coming out of that plane) [88]. (Used with permission. Copyright Institute of Physics (IOP) Publishing.)

while the opposing counterclockwise shear only has the short axis to work with – then one rotation will win over the other and the object can be turned clockwise in a controlled fashion. This works for any object that is not fully symmetric. For example, a sphere, which is fully rotationally symmetric, will not be turned as depicted in the second panel of the figure. However, the ellipsoid, shown in the third panel, can be turned by an irrotational saddle flow.

In Fig. 9.34 we show initial results for position and orientation control of an ellipsoidal object in the plane in simulations. The fluid dynamics in the device is the same as before. Also, as before, there is a linear mapping from electrode actuations to object configuration velocity, here to its translation and rotation velocities. For any location and orientation of the ellipsoid, this mapping can be inverted by least-squares to find the electrode actuations that will move and rotate the object from where it is to where it should be. For even less symmetric objects than ellipsoids, like helixes, there will be coupling between translational and rotational motion. In that case a linear mapping between the applied voltage and particle velocity still holds in principle, and consequently control should still be possible in a
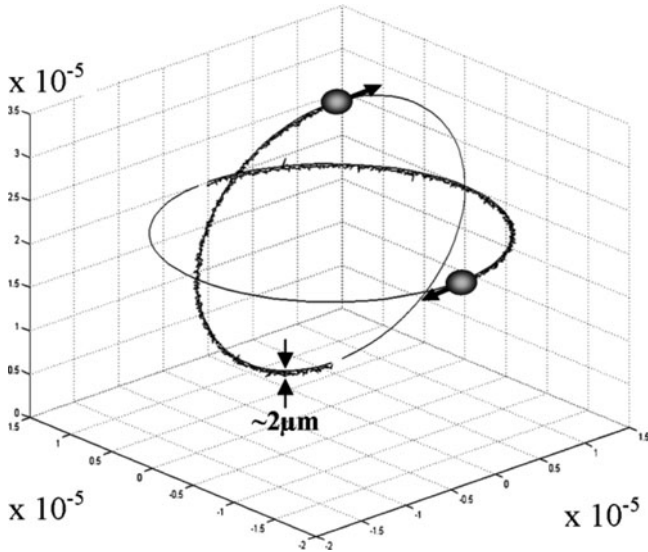
Fig. 9.32 Two nanoparticles (diameter 10 nm) controlled simultaneously in the presence of Brownian motion and a 50% charge uncertainty [88]. (Used with permission. Copyright Institute of Physics (IOP) Publishing.)
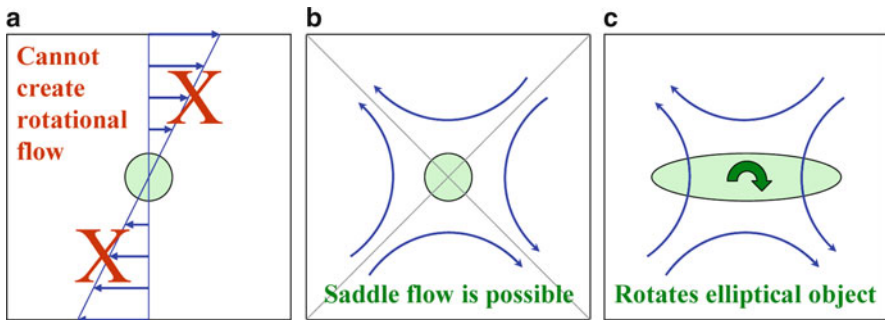
Fig. 9.33 Flow actuation to turn a nonspherical object (the shown flow would be in addition to flow being used to translate the object). (**a**) It is not possible to create the illustrated unidirectional shear flow since that flow is rotational. In the devices the flow follows the electric field which is always irrotational. However, a saddle flow can be created in the device. A saddle flow will not turn a fully rotationally symmetric object like a sphere (**b**) but it will turn an object with less rotational symmetry like the ellipsoid (**c**)

similar least-squares inversion fashion. A further description of our rotation control simulation efforts can be found in [115]. Experiments to test flow control of object translation and orientation are currently underway and will be reported in future publications.
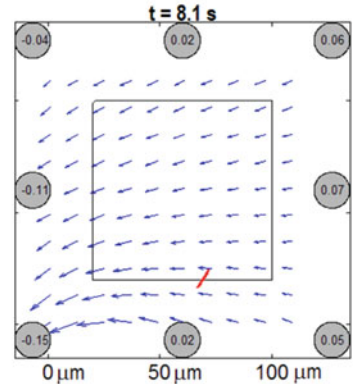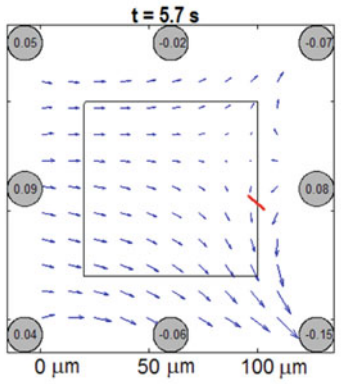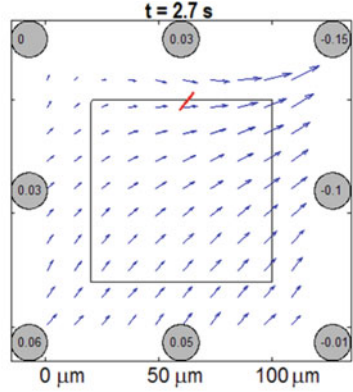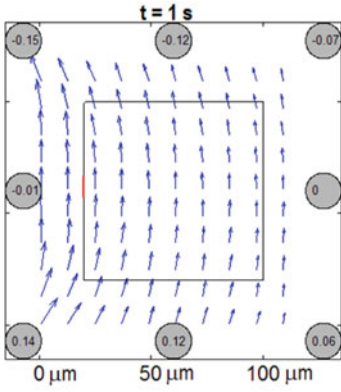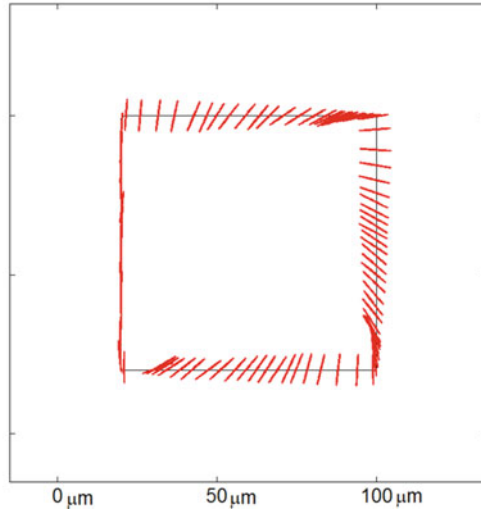
9.4 Conclusion

Feedback control has enabled microfluidic devices, here electrowetting-on-dielectric as well as simple PDMS devices, to carry out new tasks robustly and with unexpected precision. We show in simulations that smart control can enable EWOD systems to manipulate single particles, and we show that cheap and easy to fabricate PDMS devices with standard electro-osmotic actuation can steer and trap one and multiple particles experimentally. Our control results have enabled nanometer precision placement of quantum dots on photonic crystals for creating multidot quantum information devices, something that has not been achieved using any other particle manipulation technique.

All our control results, for the two examples in this chapter and for other examples in our research (e.g., magnetic control for directing drugs to tumors [116–118]), have been and are being enabled by detailed physical modeling. Especially for new physical situations, this modeling is difficult and time consuming (our modeling effort for electrowetting has continued over many years), but in every case it has enabled us to create controllers that far exceed the performance that would have been possible without modeling. In situations where we deal with chemistry, new physics, and complex samples (fluids that can be solidified with light, living cells, and human samples), we have to choose carefully what to model. Often we are not able to list, let alone mathematically describe in detail, all the relevant physical phenomena; yet we must model enough key physics so that the control algorithm can know how to make things better at each time. To identify the key physics and find the right modeling balance is one of our major challenges.

In terms of control algorithm design, defining a tractable mathematical control problem is the most critical step. It is easy to state a control problem that is clearly useful and we would like to solve, e.g., control of nonlinear partial differential equations through their moving boundary conditions, but that will not admit a useable solution in the foreseeable future. Instead, we try to define more specific problems that are still relevant but that can be solved, and then to build up our expertise to more general domains. For example, for control of electrowetting, the critical insight was that there is a linear mapping from the pressures created by the electrode pads to the particle velocities. This linear mapping reduced the control problem to a least-squares inversion of the small linear matrix map

---

Fig. 9.34 Position and orientation control of an ellipsoid in the plane by electro-osmotic flow control using eight electrodes. The ellipsoid is controlled to start at the bottom left corner of the desired trajectory, trace the square path, and then return to the bottom left corner. Along each of the four segments of the desired trajectory, the orientation task is to align the major axis of the ellipsoid along that segment by the time it reaches the end of that segment. The ellipsoid is perturbed by translational and rotational thermal (Brownian) motion. *Top*: Four time snapshots are shown (electrode actuation voltages are shown by the values in the *gray circles*, the resulting EO flow field is shown by the *arrows*). *Bottom*: The resulting sequence of ellipsoid positions and orientations is shown for 95 times. (Used with permission. Copyright Institute of Physics (IOP) Publishing.)

from the pressures to the velocities (9.9), after which we corrected for the static nonlinear relationship between the applied voltages and the pressures they create. The least-squares matrix problem, unlike a more general nonlinear PDE control with moving boundary conditions problem, is tractable and can be solved in real-time with minimal computational power. It made control implementation practical for electrowetting.

As in the electrowetting example, we are always trying to map from application needs through our modeling to available or possible control design schemes. For example, an application task (such as putting these living cells here) must be translated through the language of modeling into tractable control schemes (e.g., least-squares, feedback linearization). In cases where existing control schemes remain insufficient for all reasonable formulations of the problem, as has turned out to be the case for focusing of magnetic drugs to deep tumors, we have to invent new control methods. In this case we must define a new control question that we believe has a hope of being answered tractably. (For magnetic drug targeting we have whittled the drug focusing goal down to a sequence of quadratic maps from magnet control inputs to desired drug distributions: now semidefinite programming tools can be used to find an optimal control at each time [119].) Achieving the right balance between the needs of the application and tractable control approaches is our second great challenge.

Finally, our third and most important challenge has been learning to communicate and effectively interact with microfabricators, chemists, physicists, biologists, clinicians, and doctors. Without them the results above would not have been possible and, more importantly, would have been without purpose.

References

1. M.A. Northrup, et al. *A Miniature analytical instrument for nucleic acids based on micromachined silicon reaction chambers. Analytical Chemistry*, 1998. **70**(5): p. 918–922.
2. R. Jabeen, et al. *Capillary electrophoresis and the clinical laboratory. Electrophoresis*. **27**(12): p. 2413–2438.
3. D. Figeys. *Adapting arrays and Lab-on-a-chip technology for proteomics. Proteomics*, 2002. **2**(4): p. 373–382.
4. J. Seo, et al. *Integrated multiple patch-clamp array chip via lateral cell trapping junctions. Applied Physics Letters*, 2004. **84**(11): p. 1973–1975.
5. G. Spera. *Implantable pumps improve drug deliver, strengthen weak hearts*. Medical Devices & Diagnostic Industry Magazine, 1997.

6. M. Gad-el-Hak, ed. *MEMS: Design and fabrication* 2ed. The MEMS handbook. Vol. 2. 2006, CRC Press, Taylor and Francis Group. 664.

7. C.T. Leondes, ed. *Fabrication Techniques for MEMS/NEMS*. MEMS/NEMS handbook. 2006, Springer: New York, NY.

8. K.E. Herold and A. Rasooly, eds. *Fabrication and microfluidics*. Lab on a chip technology. Vol. 1. 2009, Caister Academic Press Norfolk, UK. 409.

9. C.A. Mack. *Fundamental principles of optical lithography: The science of microfabrication*. 2008, West Sussex, England: John Wiley and Sons Ltd. 534.

10. M. Meyyappan. *A review of plasma enhanced chemical vapour deposition of carbon nanotubes. Journal of Physics D-Applied Physics*, 2009. **42**(21).

11. R. Bogwe. *Self-assembly: a review of recent developments. Assembly Automation*, 2008. **28**(3): p. 211–215.

12. J.C. Huie. *Guided molecular self-assembly: a review of recent efforts. Smart Materials & Structures*, 2003. 12(2): p. 264–271.

13. S.D. Minteer, ed. *Microfluidic Techniques: Reviews and protocols (Methods in molecular biology)*. Methods in molecular biology. Vol. 321. 2005, Humana Press: Clifton, New Jersey. 247.

14. P. Kim, et al. *Soft lithography for microfluidics: a review. Biochip Journal*, 2008. **2**(1): p. 1–11.

15. R.L. Panton. *Incompressible flow*. 2 ed. 1996, New York, NY: John Wiley & Sons, Inc.

16. G.E. Karniadakis and A. Beskok. *Micro flows: Fundamentals and simulation*. 2001, New York, NY: Springer Verlag.

17. A. Beskok. *Physical challenges and simulation of micro fluidic transport*. in *39th Aerospace Sciences Meeting & Exhibit*. 2001. Reno, Nevada: AIAA.

18. M. Gad-el-Hak. *The fluid mechanics of microdevices – The freeman scholar lecture. Journal of Fluids Engineering*, 1999. **121**: p. 5.

19. S. Walker and B. Shapiro. *Modeling the fluid dynamics of electro-wetting on dielectric (EWOD). Journal of Micro-Electro-Mechanical Systems*, 2006. **15**(4): p. 986–1000.

20. S. Chaudhary and B. Shapiro. *Arbitrary steering of multiple particles at once in an electroosmotically driven microfluidic system. IEEE Transactions on Control Systems Technology*, 2006. **14**(4): p. 669–680.

21. L. Pauling. *General chemistry*. 1970, New York: Dover Publications, Inc.

22. S.R. Quake and T.M. Squires. *Microfluidics: Fluid physics at the nanoliter scale. Reviews of Modern Physics*, 2005. bf 77(3): p. 977–1026.

23. M.H. Oddy, J.G. Santiago, and J.C. Mikkelson. *Electrokinetic instability micromixing. Analytical Chemistry*, 2001. **73**(24): p. 5822–32.

24. J. Fowler, H. Moon, and C.J. Kim. *Enhancement of mixing by droplet-based microfluidics*. IEEE Conf. MEMS, Las Vegas, NV, 2002: p. 97–100.

25. I. Glasgow and N. Aubry. *Enhancement of microfluidic mixing using time pulsing. Lab on a Chip*, 2003. **3**(2): p. 114–120.

26. K.J. Astrom and R.M. Murray. *Feedback systems: An introduction for scientists and engineers*, 2006. Princeton University Press. 2008.

27. J.C. Doyle, B.A. Francis, and A.R. Tannenbaum. *Feedback control theory*. 1992, New York, NY: Macmillan Publishing Company.

28. R.M. Murray, et al. *Control in an information rich world*. 2002, Air Force Office of Scientific Research (AFOSR).

29. F. Mugele and J. Baret. *Electrowetting: from basics to applications. journal of physics: condensed matter*, 2005. **17**: p. R705–R774.

30. J. Lee, et al. *Electrowetting and electrowetting-on-dielectric for microscale liquid handling. Sensor Actuat. A-Phys*, 2002. **95**: p. 269.

31. S. Fusayo, et al. *Electrowetting on dielectrics (EWOD): Reducing voltage requirements for microfluidics. Polymeric Materials: Science & Engineering*, 2001. **85**: p. 12–13.

32. H. Ren, et al. *Dynamics of electro-wetting droplet transport. Sensors and Actuators B-Chemical*, 2002. **87**(1): p. 201–206.

33. E. Seyrat and R.A. Hayes. *Amorphous fluoropolymers as insulators for reversible low-voltage electrowetting. Journal of Applied Physics*, 2001. **90**(3).
34. R.A. Hayes and B.J. Feenstra. *Video-speed electronic paper based on electrowetting. Nature*, 2003. **425**(6956): p. 383–385.
35. T. Roques-Carmes, R.A. Hayes, and L.J.M. Schlangen. *A physical model describing the electro-optic behavior of switchable optical elements based on electrowetting. Journal of Applied Physics*, 2004. **96**(11): p. 6267–6271.
36. T. Roques-Carmes, et al. *Liquid behavior inside a reflective display pixel based on electrowetting. Journal of Applied Physics*, 2004. **95**(8): p. 4389–4396.
37. B. Berge and J. Peseux. *Variable focal lens controlled by an external voltage: An application of electrowetting. European Physical Journal E*, 2000. **3**(2): p. 159–163.
38. C. Quilliet and B. Berge. *Electrowetting: a recent outbreak. Current Opinion in Colloid & Interface Science*, 2001. **6**(1): p. 34–39.
39. S.K. Cho, H. Moon, and C.J. Kim. *Creating, transporting, cutting, and merging liquid droplets by electrowetting-based actuation for digital microfluidic circuits. Journal of Microelectromechanical Systems*, 2003. VOL. **12**(NO. 1): p. 70–80.
40. M.G. Pollack, R.B. Fair, and A.D. Shenderov. *Electrowetting-based actuation of liquid droplets for microfluidic applications. Applied Physics Letters*, 2000. **77**(11).
41. H.J.J. Verheijen and W.J. Prins. *Reversible electrowetting and trapping of charge: Model and experiments. Langmuir*, 1999. **15**: p. 6616–6620.
42. B. Berge. *Electrocapillarity and wetting of insulator films by water. Comptes Rendus de l Academie des Sciences Series II*, 1993. **317**(2): p. 157–163.
43. B. Shapiro, et al. *Equilibrium behavior of sessile drops under surface tension, applied external fields, and material variations. Journal of Applied Physics*, 2003. **93**(9).
44. M. Armani, et al. *Control of micro-fluidic systems: Two examples, results, and challenges. International Journal of Robust and Nonlinear Control.*, 2005. **15**(16): p. 785–803.
45. S.W. Walker, B. Shapiro, and R.H. Nochetto. *Electrowetting with contact line pinning: Computational modeling and comparisions with experiments. Physics of Fluids*, 2009. **23**(10): p. 102103.
46. K. Zhou, J.C. Doyle, and K. Glover. *Robust and optimal control*. 1996: Prentice Hall, New Jersey.
47. A. Isidori. *Nonlinear control systems*. 3 ed. Communications and control engineering. 1995: Springer.
48. G. Lippmann. *Relation entre les phenomenes electriques et capillaires. Ann. Chim. Phys.*, 1875. **5**: p. 494–549.
49. R.F. Probstein. *Physicochemical Hydrodynamics: An introduction*. 2 ed. 1994, New York: John Wiley and Sons, Inc.
50. P.C. Hiemenz and R. Rajagopalan. *Principles of colloid and surface chemistry*. 3 ed. 1997, New York, Basel, Hong Kong: Marcel Dekker, Inc.
51. R.P. Feynman, R.B. Leighton, and M. Sands. *The feynman lectures on physics*. 1964: Addison-Wesley Publishing Company.
52. S.W. Walker. *Modeling, simulating, and controlling the fluid dynamics of electro-wetting on dielectric, in aerospace engineering*. 2007, University of Maryland: College Park.
53. H.W. Lu, et al. *A diffuse interface model for electrowetting droplets in a hele-shaw cell. J. Fluid Mech*, 2007. **590**: pp. 411–435.
54. H.S. Hele-Shaw. *The flow of water. Nature*, 1898. **58**: p. 34–35.
55. G.K. Batchelor. *An Introduction to fluid dynamics*. 1967: Cambridge University Press.
56. M.P. do Carmo. *Differential geometry of curves and surfaces*. 1976, Upper Saddle River, New Jersey: Prentice Hall.
57. T.D. Blake. *The physics of moving wetting lines. Journal of Colloid and Interface Science*, 2006. **299**: p. 1–13.
58. S. Osher and R. Fedkiw. *Level set methods and dynamic implicit surfaces*. 2003: Springer-Verlag New York.

59. S.A. Sethian. *Level set methods & fast marching methods*. 2 ed. 1999: Cambridge University Press.
60. R. Caiden, R. Fedkiw, and C. Anderson. *A numerical method for two phase flow consisting of separate compressible and incompressible regions. J. Comput. Phys.*, 2001. **166**: p. 1–27.
61. P. Smereka. *Semi-implicit level set methods for curvature and surface diffusion motion. Journal of Scientific Computing*, 2003. **19**(1–3): p. 439–456.
62. W.J. Rider and D.B. Kothe. *Stretching and tearing interface tracking methods, in 12th AIAA CFD Conference*. 1995.
63. H.C. Kuhlmann and H.J. Rath. *Free surface flows 1ed*. CISM courses and lectures, international centre for mechanical sciences. Vol. **39**, New York, NY: Springer. 300.
64. D. Enright, R. Fedkiw, J. Ferziger, I. Mitchell. *A hybrid particle level set method for improved interface capturing. Journal of Computational Physics*, 2002. **183**: p. 83.
65. F. Losasso, F. Gibou, R. Fedkiw. *Simulating water and smoke with an octree data structure. in ACM Trans. Graph. (SIGGRAPH Proc.)*. 2004.
66. X. Yang, et al. *An adaptive coupled level-set/volume-of-fluid interface capturing method for unstructured triangular grids. Journal of Computational Physics* 2006. **217**(2): p. 364–394
67. S.W. Walker. *A hybrid variational-level set approach to handle topological changes, in mathematics*. 2007, University of Maryland: College Park.
68. C.J. Kim. *Micropumping by electrowetting. in Int. mechanical engineering congress and exposition, New York, NY, IMECE2001/HTD-24200*. 2001.
69. V. Srinivasan, V. Pamula, M. Pollack, and R. Fair. *A digital microfluidic biosensor for multianalyte detection. in Proceedings of the IEEE 16th Annual International Conference on Micro Electro Mechanical Systems*. 2003.
70. P. Paik, V.K. Pamula, and R.B. Fair. *Rapid droplet mixers for digital microfluidic systems. Lab on a Chip*, 2003. **3**: p. 253–259.
71. S.K. Cho, H. Moon, J. Fowler, S.K. Fan, and C.J. Kim. *Splitting a liquid droplet for electrowetting-based microfluidics. in Int. mechanical engineering congress and exposition, New York, NY, IMECE2001/MEMS-23831*. 2001.
72. S. Walker and B. Shapiro. *A control method for steering individual particles inside liquid droplets actuated by electrowetting. Lab on a Chip*, 2005. **12**(1): p. 1404–1407.
73. F.L. Lewis, and V.L. Syrmos. *Optimal control*. 2nd ed. 1995, New York, NY: Wiley-Interscience. 560.
74. K.W. Morton, and D.F. Mayers. *Numerical solution of partial differential equations*. 1994: Cambridge University Press. 239.
75. G. Strang. *Linear algebra and its applications*. 3 ed. 1988, New York, NY: Brooks Cole. 520.
76. E.C. Zachmanoglou and D.W. Thoe. *Introduction to partial differential equations with applications*. 1986, New York, NY: Dover Publications, Inc.
77. A. Ralston, and P. Rabinowitz. *A first course in numerical analysis*. 2nd ed. 2001, Mineola, NY: Dover.
78. L. Jauffred, A.C. Richardson, and L.B. Oddershede. *Three-dimensional optical control of individual quantum dots. Nano Letters*. **8**(10): p. 3376–3380.
79. A. Ashkin, et al. *Observation of a single-beam gradient force optical trap for dielectric particles. Optics Letters*. **11**(5): p. 288–290.
80. C. Pei-Yu, et al. *Light-actuated AC electroosmosis for nanoparticle manipulation. Microelectromechanical Systems, Journal of.* **17**(3): p. 525–531.
81. A.H.J. Yang, et al. *Optical manipulation of nanoparticles and biomolecules in sub-wavelength slot waveguides. Nature.* **457**(7225): p. 71–75.
82. A. Ashkin. *History of optical trapping and manipulation of small-neutral particles, atoms, and molecules. IEEE Journal on Selected Topics in Quantum Electronics*, 2000. **6**(6): p. 841–856.
83. M. Armani, et al. *Using feedback control and micro-fluidics to independently steer multiple particles. Journal of Micro-Electro-Mechanical Systems*, 2006. **15**(4): p. 945–956.
84. C. Ropp, et al. *Manipulating quantum dots to nanometer precision by control of flow. Nano Letters*, 2010. **10**(7): p. 2525–2530.

85. K.C. Neuman and A. Nagy. *Single-molecule force spectroscopy: optical tweezers, magnetic tweezers and atomic force microscopy. Nat Meth.* **5**(6): p. 491–505.

86. H. Zhang and K.K. Liu. *Optical tweezers for single cells. Journal of the Royal Society, Interface/the Royal Society.* **5**(24): p. 671–690.

87. F. Qian, et al. *Combining optical tweezers and patch clamp for studies of cell membrane electromechanics. Review of Scientific Instruments.* **75** (9): p. 2937–2942.

88. R.Probst, B.Shapiro, *3-dimensional electrokinetic tweezing: Device design, modeling, and control algorithms*, Journal of Micromechanics and Microengineering, 2011 **21**(2)

89. C. Ropp, et al. *Positioning and immobilization of individual quantum dots with nanoscale precision. Nano Letters*, 2010. **10** p. 4673–4679.

90. L.E. Locascio, C.E. Perso, and C.S. Lee. *Measurement of electroosmotic flow in plastic imprinted microfluid devices and the effect of protein adsorption on flow rate. Journal of Chromotography A*, 1999. **857**: p. 275–284.

91. D.J. Harrison, et al. *Micromachining a miniaturized capillary electrophoresis-based chemical-analysis system on a chip. Science*, 1993. **261**(5123): p. 895–897.

92. A. Manz, et al. *Electroosmotic pumping and electrophoretic separations for miniaturized chemical-analysis systems. Journal of Micromechanics and Microengineering*, 1994. **4**(4): p. 257–265.

93. W. Korohoda and A. Wilk. *Cell electrophoresis — a method for cell separation and research into cell surface properties. Cellular & Molecular Biology Letters.* **13**(2): p. 312–326.

94. J.N. Mehrishi and J. Bauer. *Electrophoresis of cells and the biological relevance of surface charge. Electrophoresis.* **23**(13): p. 1984–1994.

95. G.G. Slivinsky, et al. *Cellular electrophoretic mobility data: A first approach to a database. Electrophoresis.* **18**(7): p. 1109–1119.

96. F. Schonfeld. *CμFD – Case study: Flow patterning by phase-shifted electroosmotic flows, in comsol user's conference* 2006: Frankfurt, Germany.

97. S. Chaudhary and B. Shapiro. *Arbitrary steering of multiple particles at once in an electroosmotically driven micro fluidic system. IEEE Trans. on Control Systems Technologies*, 2005: 14669–680.

98. T. Zhou, et al. *Time-dependent starting profile of velocity upon application of external electrical potential in electroosmotic driven microchannels. Colloids and Surfaces A: Physicochemical and Engineering Aspects*, 2006. **277** (1–3): p. 136–144.

99. D. Yan, et al. *Visualizing the transient electroosmotic flow and measuring the zeta potential of microchannels with a micro-PIV technique. The Journal of Chemical Physics.* **124**(2): p. 021103–4.

100. M.A. Henderson. *The interaction of water with solid surfaces: fundamental aspects revisited. Surface Science Reports*, 2002. **46**(1–8): p. 1–308.

101. J. Lyklema, et al. *Fundamentals of interface and colloid science*.

102. M. Armani, et al. *Using feedback control and micro-fluidics to steer individual particles. in 18th IEEE International Conference on Micro Electro Mechanical Systems*. 2005. Miami, Florida.

103. I. Rodriguez and N. Chandrasekhar. *Experimental study and numerical estimation of current changes in electroosmotically pumped microfluidic devices. Electrophoresis*, 2005. **26**(6): p. 1114–1121.

104. A. Badolato, et al. *Deterministic coupling of single quantum dots to single nanocavity modes. Science.* **308**(5725): p. 1158–1161.

105. K. Hennessy, et al. *Quantum nature of a strongly coupled single quantum dot-cavity system. Nature.* **445**(7130): p. 896–899.

106. D. Englund, et al. *Controlling cavity reflectivity with a single quantum dot. Nature.* **450**(7171): p. 857–861.

107. A.V. Akimov, et al. *Generation of single optical plasmons in metallic nanowires coupled to quantum dots. Nature.* **450**(7168): p. 402–406.

108. D.E. Chang, et al. *A single-photon transistor using nanoscale surface plasmons. Nat Phys.* **3**(11): p. 807–812.

109. Y. Akhane, et al. *High-Q photonic nanocavity in a two-dimensional photonic crystal. Nature*, 2003. **425**: p. 944–947.
110. Q. Zhang, et al. *Large ordered arrays of single photon sources based on II-VI semiconductor colloidal quantum dot. Opt. Express*. **16**(24): p. 19599, 19592–19599, 19592.
111. J. Liu, et al. *Controlled photopolymerization of hydrogel microstructures inside microchannels for bioassays. Lab on a Chip*. **9**(9): p. 1301–1305.
112. J.T. Fourkas and L. Li. *Multiphoton polymerization. Mater. Today*, 2007. **10**(6): p. 30–37.
113. R.E. Thompson, D.R. Larson, and W.W. Webb. *Precise nanometer localization analysis for individual fluorescent probes. Biophysical Journal*, 2002. **82**(5): p. 2775–2783.
114. L.J. Li and J.T. Fourkas. *Multiphoton polymerization. Materials Today*, 2007. **10**(6): p. 30–37.
115. P. Mathai, A. Berglund, A. Liddle, B. Shapiro, *Simultaneous positioning and orientation of a single nano-object by flow control*, New Journal of Physics, **13**: p. 013027, 19 January 2011.
116. B. Shapiro, et al. *Control to concentrate drug-coated magnetic particles to deep-tissue tumors for targeted cancer chemotherapy. in 46th IEEE Conference on Decision and Control*. 2007. New Orleans, LA.
117. B. Shapiro, et al. *Dynamic control of magnetic fields to focus drug-coated nano-particles to deep tissue tumors, in 7th International Conference on the Scientific and Clinical Applications of Magnetic Carriers*. 2008: Vancouver, British Columbia.
118. B. Shapiro. *Towards dynamic control of magnetic fields to focus magnetic carriers to targets deep inside the body. Journal of Magnetism and Magnetic Materials*, 2009. **321**(10): p. 1594–1599.
119. A.Komaee and B.Shapiro, *Magnetic steering of a distributed ferrofluid towards a deep target with minimal spreading, In 50th IEEE Conference on Decision and Control and European Control Conference (CDC-ECC)*. Dec 2011. Orlando, FL.